https://doi.org/10.5194/acp-2021-516
Preprint. Discussion started: 14 July 2021

Atmospheric Chemistry and Physics Discussions

Chemically speciated mass size distribution, particle effective density and origin of non-refractory PM_1 measured at a rural background site in Central

Petra Pokorná[1], Naděžda Zíková[1], Radek Lhotka[1,2], Petr Vodička[1], Saliou Mbengue[3], Adéla Holubová Šmejkalová[4], Véronique Riffault[5], Jakub Ondráček[1], Jaroslav Schwarz[1], Vladimír Ždímal[1]

[1]Department of Aerosol Chemistry and Physics, Institute of Chemical Process Fundamentals, Czech Academy of Sciences, Rozvojová 135/1, 165 02 Prague, Czech Republic

[2]Institute for Environmental Studies, Faculty of Science, Charles University, Benátská 2, 128 01 Prague 2, Czech Republic

[3]Global Change Research Institute, Czech Academy of Sciences, Bělidla 986/4a, 603 00 Brno, Czech Republic

[4]Czech Hydrometeorological Institute, Air Quality Division, Na Šabatce 2050/17, 143 06 Prague, Czech Republic

[5] IMT Lille Douai, Institut Mines-Télécom, Université de Lille, Centre for Energy and Environment, F-59000 Lille, France

Correspondence to: Petra Pokorná (pokornap@icpf.cas.cz)

Abstract

The seasonal variability of non-refractory PM_1 (NR-PM_1) was studied at a rural background site (National Atmospheric Observatory Košetice – NAOK) in the Czech Republic to examine the impact of atmospheric regional and long-range transport in Central Europe. NR-PM_1 measurements were performed by compact time-of-flight aerosol mass spectrometry (C-ToF-AMS), and the chemically speciated mass size distributions, effective density, and origin were discussed. The average PM_1 concentrations, calculated as the sum of the NR-PM_1 (after collection efficiency corrections – CE corrections of 0.4 and 0.33 in summer and winter, respectively) and the equivalent black carbon (eBC) concentrations measured by an aethalometer (AE), were 8.58 ± 3.70 μg m^{-3} in summer and 10.08±8.04 μg m^{-3} in winter. Organics dominated during both campaigns (summer/winter: 4.97 ± 2.92/4.55± 4.40 μg m^{-3}), followed by SO_4^{2-}in summer (1.68 ± 0.81/1.36± 1.38 μg m^{-3}) and NO_3^- in winter (0.67 ± 0.38/2.03 ± 1.71 μg m^{-3}). The accumulation mode dominated the average mass size distribution during both seasons, with larger particles of all species measured in winter (mode diameters: Org: 334/413 nm, NO_3^-: 377/501 nm, SO_4^{2-}: 400/547 nm, and NH_4^+: 489/515 nm) pointing to regional and long-range transport. However, since the winter aerosols were less oxidized than the summer aerosols (comparing fragments f_{44} and f_{43}), the importance of local sources in the cold part of the year was not negligible. The average PM_1 particle effective density, defined as the ratio of the mass to the volume of a particle, corresponded to higher inorganic contents during both seasons (summer: ~1.30 g cm^{-3} and winter: ~1.40 g cm^{-3}). However, the effective densities during episodes of higher mass concentrations calculated based on the particle number (mobility diameter) and mass size distribution (vacuum aerodynamic diameter) were even higher, ranging from 1.40 – 1.60 g cm^{-3} in summer and from 1.40 – 1.75 g cm^{-3} in winter. Although aged continental air masses from the SE were rare in summer (7%), they were

https://doi.org/10.5194/acp-2021-516
Preprint. Discussion started: 14 July 2021

connected with the highest concentrations of all NR-PM_1 species, especially SO_4^{2-} and NH_4^+. In winter, slow continental air masses from the SW (44%) were linked to inversion conditions over Central Europe and were associated with the highest concentrations among all NR-PM_1 measurements.

1. Introduction

Studies on airborne particulate matter (PM) are needed to better understand its temporal and spatial variations, atmospheric processing, long-term trends, adverse health and environmental consequences, and pollution sources (Putaud, et al., 2004; Tørseth et al., 2012; Belis et al., 2013; EEA 2019). Aerosol particles can be characterized by many different properties such number concentration, mass concentration, particle size, mass, volume, density, etc. Particle density is an important physical property of atmospheric particles and is linked to particle emission sources and atmospheric physical and chemical ageing processes. The effective density, which is defined as the ratio of the mass of the particle to its apparent volume, assuming a spherical particle, and can be estimated by comparing the size distributions of the aerodynamic and mobility diameters, is a quantity reflecting the physiochemical properties of aerosol particles (e.g., DeCarlo 2004; Pitz et al., 2003, 2008; Hu et al., 2012; Qiao et al., 2018).

Over the last decades, a growing number of scientific studies have investigated the detailed chemical composition of PM with variable temporal resolutions (1, 12, and 24 hours or higher) using offline filter analyses (Putaud et al., 2010; Watson and Chow, 2011). Nowadays, online methods with high temporal resolutions (30 min and less) are available, as aerosol mass spectrometers (AMSs) are utilized that quantitatively measure chemical composition as well as the chemically resolved size distributions of submicron non-refractory PM (NR-PM_1) (Jayne et al., 2000; Jimenez et al., 2003). Although measuring the seasonal variability of NR-PM_1 is becoming more common (Bressi et al., 2021), systematic studies considering chemically speciated mass size distributions are still rare. The available studies have also focused on new particle formation and growth, temporal variations, and the origin and sources of particles, including results presented from urban (Drewnick et al., 2004; Dall'Osto et al., 2009; Hersey et al., 2011; Freutel et al., 2013; Salimi et al., 2015; Kubelová et al., 2015), forestry (Allan et al., 2006), mid-altitude (Freney et al. 2011) and rural (Poulain et al., 2011; Milic et al., 2017) background environments.

Measurements obtained at rural background sites that are representative of wider areas are important for investigating the influence of regional and long-range transport as well as the long-term trends in PM characteristics. In the Czech Republic, the National Atmospheric Observatory Košetice (NAOK), officially classified as a Central European rural background site, is involved in the European Monitoring and Evaluation Programme (EMEP), Aerosol, Clouds, and Trace Gases Research Infrastructure Network (ACTRIS), and Global Atmosphere Watch (GAW) network. This site has been characterized in terms of the local $PM_{2.5}$ chemical composition and seasonal variability (Schwarz et al., 2016), the PM_1 isotopic composition (Vodička et al., 2019) and the PAH_S that are bound to PM_1 (Křůmal and Mikuška, 2020). Studies conducted at NAOK have also characterized the long-term trends of atmospheric carbonaceous aerosols (Mbengue et al., 2018, 2020) and $PM_{2.5}$ elemental compositions and sources (Pokorná et al., 2018). The particle number size distribution (PNSD) and influence of in-cloud and below-cloud scavenging have been investigated with long-term measurements by

https://doi.org/10.5194/acp-2021-516
Preprint. Discussion started: 14 July 2021

Zíková and Ždímal (2013, 2016). However, detailed work focused on the seasonal variability in PM chemical composition data with high temporal and spatial resolutions is still lacking at this site.

Therefore, this paper aims to assess NR-PM_1 (organics, sulphate, nitrate, ammonium and chloride) based on the chemically speciated mass size distribution, particle effective density, and origin during intensive campaigns in summer and winter at NAOK.

2. Materials and methods

2.1 Instrumentation

Two intensive sampling campaigns were carried out in July 2019 (1.7. – 31.7.) and in January-February 2020 (16.1. – 10.2.) at NAOK. During the campaigns, several physical and chemical atmospheric aerosol properties were measured together with complete meteorological data collected from a professional meteorological station (WMO station 11628).

The size-resolved NR-PM_1 chemical composition (the sum of organic, sulphate, nitrate, ammonium and chloride) was measured by a compact time-of-flight aerosol mass spectrometer (C-ToF-AMS, Aerodyne, USA, Drewnick et al., 2005) with a 5-min temporal resolution. The instrument was connected to an inlet consisting of a $PM_{2.5}$ sampling head (16.7 l min^{-}) and a Nafion dryer (Perma Pure MD-110-24P-4). Isokinetic sub-sampling was used to split the flow into AMS (0.1-l min) from the main flow. The AMS size, flow, and ionization efficiency (IE) calibrations were performed in the brute-force single-particle mode (BFSP, Drewnick et al., 2005, monodisperse 350-nm ammonium nitrate aerosol particles) at the beginning of each campaign. Additionally, the measurements were performed with a HEPA filter applied to the inlet to account for zero-value measurements and to adjust the fragmentation table (Allan et al., 2004).

Additionally, 12-h PM_1 filter samples were collected by a sequential Leckel LVS-3 (Sven Leckel Ingenieurbüro, Germany) for subsequent chemical analyses of cations, anions and monosaccharide anhydrides using ion chromatography (Dionex ICS-5000+ system, Sunnyvale, CA, USA). More details about the methods can be found in Kozáková et al., 2019.

The particle number concentration (PNC) and particle number size distribution (PNSD) were measured every 5 min by a mobility particle size spectrometer (MPSS, IFT TROPOS, Germany, with CPC 3772, TSI USA) in the size range of 10 – 800 nm (a detailed description of the measurement set-up can be found in Zíková and Ždímal, 2013). The cumulative particle number concentrations over seven size ranges (10 – 25 nm, 25 – 50 nm, 50 – 80 nm, 80 – 150 nm, 150 – 300 nm, 300 – 800 nm, and 10 – 800 nm) were subsequently calculated from the PNSD. Additionally, the 1-h $PM_{2.5}$ mass concentrations were measured using a beta-gauge (MP101M, Environement SA, France).

The concentrations of equivalent black carbon (eBC) were estimated using a 7-wavelength aethalometer (Model AE33, Magee Scientific, Berkeley, CA, USA) sampling through a PM_{10} sampling head (Leckel GmbH) with a 1-min temporal resolution. Additionally, 4-h $PM_{2.5}$ online organic and elemental carbon (OC/EC) concentrations (Sunset Laboratory Inc., USA) were measured following the shortened EUSAAR2 protocol (Cavalli et al., 2010).

https://doi.org/10.5194/acp-2021-516
Preprint. Discussion started: 14 July 2021

2.2 Data analysis

The standard data processing procedure of AMS data (i.e., m/z calibration, baseline subtraction, and air beam correction) was carried out by running the Squirrel v1.62 program in Igor Pro data analysis software (WaveMetrics, Inc.).

The statistical data treatment was performed using R version 3.6.1 (R Core Team, 2019) with the ggplot2 (Wickham, 2016) and Openair (Carslaw and Ropkins, 2012) packages.

2.2.1 Collection efficiency determination

To determine the collection efficiency (CE; Drewnick et al., 2005) in the AMS, PM_1 filter sampling with subsequent ion chromatography (IC) analysis was conducted in parallel with the AMS measurements. A comparison between the sulphate concentrations measured by AMS and by IC revealed the better suitability of the CE corrections for summer (CE = 0.40; y = 0.99x, R^2 = 0.95) as well as for winter (CE = 0.33; y = 1.00x, R^2 = 0.81) in comparison to the composition-dependent CE correction (CDCE; Middlebrook et al., 2012) shown in Fig. A1. Therefore, CE correction was applied to the AMS data for both seasons to maintain consistency in the data corrections. Similarly, using the same methodology, seasonal CE corrections (summer CE = 0.29 and winter CE = 0.35) were also successfully applied to AMS data measured at a suburban site in Prague (Kubelová et al., 2015).

2.2.2 Particle effective density calculation

Two approaches were employed to calculate the particle effective density. In the first approach, AMS data representing the mass size distributions based on the vacuum aerodynamic diameter (D_{va}) in the size range from 10 to 7000 nm (calculated in Squirrelu software; 50 – 800 nm in reality) and MPSS data representing the dN/dlog D_p in the size range from 11.3 to 987 nm were utilized. In the MPSS data, he D_{va} were recalculated using the mobility diameters with a density of 1.5 g cm^{-3}, and the D_{va} were then recalculated back to mobility diameters with the assumption of spherical particles as in DeCarlo et al. (2004):

$$D_m = \frac{D_{va}}{\rho}\rho_0, \qquad (1)$$

where D_m is the mobility diameter, D_{va} is the vacuum aerodynamic diameter, ρ_0 is the water density, and ρ is the total density of particles, resulting in the sizes ranging from 7.53 to 658 nm. The position of the main mode was compared between the AMS and MPSS data to estimate the aerosol effective density. The density was first used to recalculate the diameters and was later also used for the mass calculations. The dN data were calculated and used for the dV and dM distribution calculations.

In the second approach, the mass concentrations of NR-PM_1 species and eBC were converted to the estimated size-dependent density (ρ) based on the following equation from Salcedo et al. (2006).

$$\rho = \frac{[Total^-_{AMS} + eBC]}{\frac{[NO_3^-]+[SO_4^{2-}]+[NH_4^+]}{1.75} + \frac{[Cl^-]}{1.52} + \frac{[Org]}{1.20} + \frac{[eBC]}{1.77}} \qquad (2)$$

The densities were assumed to be approximately 1.75 g cm^{-3} for ammonium nitrate, ammonium sulphate, and ammonium bisulphate (Lide, 1991); 1.52 g cm^{-3} for ammonium chloride (Lide,

https://doi.org/10.5194/acp-2021-516
Preprint. Discussion started: 14 July 2021

1991); 1.20 g cm^{-3} for organics (Turpin and Lim, 2001); and 1.77 g cm^{-3} for black carbon (Park et al., 2004).

2.2.3 Cluster analysis

For both campaigns, 96-hour backwards trajectories were calculated using the Hybrid Single-Particle Lagrangian Integrated Trajectory (HYSPLIT) model (Rolph et al., 2017) with a 500-m AGL starting position and Global Data Assimilation System (GDAS) Archive Information at a resolution of 1° × 1° as input data. The calculations were initialized every 6 hours. The trajectories were further clustered using Hysplit4 software based on the total spatial variance.

From HYSPLIT, the planetary boundary layer height data were extracted using the vmixing program (https://www.ready.noaa.gov/HYSPLIT_vmixing.php). For the planetary boundary layer height calculations, the 0.25° × 0.25° Global Forecast System (GFS) dataset was used as input data to obtain a 3-hour temporal resolution.

2.2.4. Episodes of high particle number and mass concentrations

To determine episodes of high particle number and mass concentrations, two approaches were utilized: i) the application of positive matrix factorization (PMF) to PNSDs and ii) the depiction of the mass size distribution of NR-PM_1 species. The episodes were studied in detail from the particle effective density and mass size distribution perspectives.

2.2.4.1 PMF on PNSD

PMF (US EPA, version PMF 5.0) was applied to the seasonal 5-min PNSDs in the range from 10 nm to 800 nm to estimate the number and profile of the PNSD factors and their contributions to the receptor. Episodes in which the factor contributions to the total particle number concentrations were higher than 80 % were chosen for the subsequent particle effective density calculations.

The input data were prepared by merging three consecutive bins to reduce the noise in the raw data, decrease the number of variables, and reduce the number of zeroes in the raw data (Leoni et al., 2018). The uncertainties were calculated according to Vu et al. (2015). The total variables were calculated by summing all the bins (N10 – 800). PMF was conducted using different uncertainty input matrices and different C3 (Vu et al., 2015) to obtain the Q_{true} closest to $Q_{expected}$; different modelling uncertainties and different numbers of factors were also applied. A C3 of 0.8 was chosen.

2.2.4.2 3D plots

The mass size distributions of nitrate, sulphate and organic matter are depicted in a colour-coded 3D plot showing episodes of high mass concentrations.

3. Results and discussions

3.1 Campaign overview

The campaigns were characterized by prevailing westerly winds with average wind speed of 3.0 ± 1.5 m s^{-1} in summer and 4.5 ± 3.1 m s^{-1} in winter (Fig. A2), average temperature of 18.5

https://doi.org/10.5194/acp-2021-516
Preprint. Discussion started: 14 July 2021

± 4.7 °C in summer and 1.4 ± 3.9 °C in winter, and negligible precipitation. The average $PM_{2.5}$ was 10.9 ± 5.9 μg m^{-3} in summer and 11.8 ± 9.9 μg m^{-3} in winter (2019 average annual concentration: 10.1 μg m^{-3}, CHMI, 2019a).

Based on the PNSD, in summer, particles in the size range of 25 – 80 nm (N25 – 50 and N50 – 80) predominated, while in winter, N80 – 150 were dominant (Table 1). Particles in the size range of 25 – 80 nm, also called the Aitken mode, are typical for rural background stations and originate from the ageing of particles generated during new particle formation (NPF) events (Costabile et al., 2009). Based on a 5-year study (2013 – 2017) evaluating PNSDs at NAOK, June and July were classified as the months with the highest NPF event frequencies (38 and 36% of days, respectively, Holubová Šmejkalová et al., 2021). The prevailing accumulation-mode particles in winter were presented in Schwarz et al., 2016, as well as in Zíková and Ždímal (2013). The average PNCs recorded during the two studied seasons were lower than the annual mean total concentration (6.6 × 10^3 cm^{-3}, Zíková and Ždímal, 2013).

Table 1. Average cumulative particle number concentrations (cm^{-3}) measured by MPSS during the summer and winter campaigns.

Size range (nm)	Summer	Winter
N10 – 25	979±1488	315±344
N25 – 50	1726±1536	529±402
N50 – 80	1112±715	478±492
N80 – 150	907±472	606±654
N150 – 300	508±191	437±368
N300 – 800	51±41	86±76
N10 – 800 (Total)	4971±2794	2451±1749

3.2 Volume and mass closure analysis with PNSD

For the mass closure analysis, the total mass concentrations measured by AMS (the sums of the organic, sulphate, nitrate, ammonium and chloride concentrations) were complemented by the eBC mass concentrations. The average PM_1 concentrations for the summer and winter campaigns were 8.58±3.70 μg m^{-3} (filter-based 12-hour PM_1 10.10 ± 6.44 μg m^{-3}) and 10.08 ± 8.04 μg m^{-3} (filter-based 12-hour PM_1 11.05 ± 7.22 μg m^{-3}), respectively. Since the PNSD (10- to 800-nm mobility diameter) was measured continuously in parallel with the eBC and NR-PM_1 mass, mass closure of the 10-min averages was performed. To do so, two approaches were utilized: i) converting the NR-PM_1 + eBC mass concentrations into volume concentrations using the composition-dependent density and ii) converting the PNSDs into mass concentrations using a constant density of 1.5 g cm^{-3}. Over the summer campaign, the NR-PM_1 + eBC volume and mass concentrations agreed well with the MPSS volume and mass concentrations in comparison to the winter campaign (Fig. 1). The seasonal effect on mass closure—already reported by Poulain et al., 2020 using ACSM at rural Melpitz, as well as by Fröhlich et al., 2015 using ToF-ACSM at Jungfraujoch could be explained by higher concentrations in larger size bins of the volume size distribution in winter compared to in summer (Fig. 2), since the AMS underestimates the particle mass concentrations for the larger size bins. This is due to the specific size cutting of each instrument and the transmission efficiency of the aerodynamic lens (Poulain et al., 2020). Moreover, the constant density is a limitation of the mass approach due to the density variability within the distinct episodes.

https://doi.org/10.5194/acp-2021-516
Preprint. Discussion started: 14 July 2021

Irregularities in the mass size distributions of nitrate, sulphate, and ammonia are discussed further in this paper.

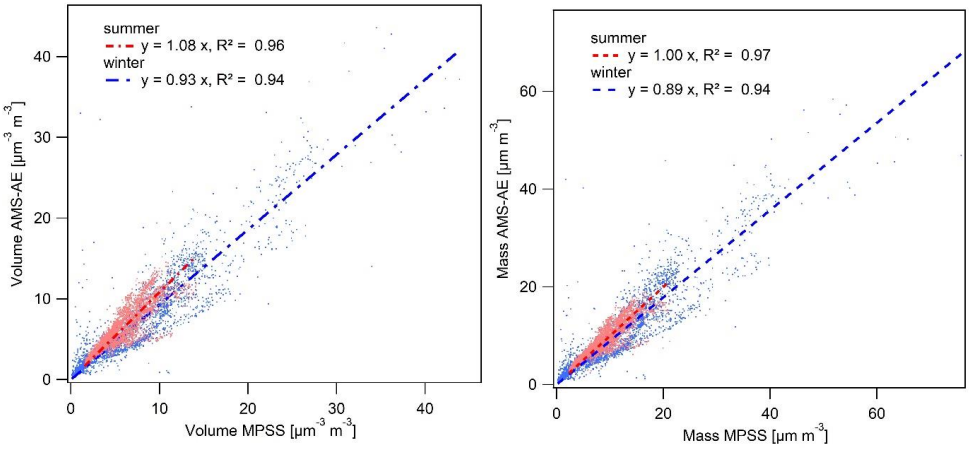

Fig. 1. Comparison between the AMS-AE and MPSS measurements during both campaigns: volume closure (left) and mass closure (right).

3.3 Concentration and origin of NR-PM$_1$

The CE-corrected mass concentrations of NR-PM$_1$ species, calculated as functions of time during the two campaigns, are shown in Fig. A3. and the seasonal average concentrations are presented in Table 2. Organics dominated during both campaigns, followed by SO_4^{2-} in summer and NO_3^- in winter. The PM$_1$ IC results confirmed higher mean SO_4^{2-} concentrations in summer ($SO_{4\,IC}^{2-}$ 1.63 ± 0.84 µg m^{-3} and $NO_{3\,IC}^-$ 0.23 ± 0.18 µg m^{-3}). However, the mean NO_3^- concentrations were slightly lower than the SO_4^{2-} concentrations in winter ($NO_{3\,IC}^-$ 0.72 ± 0.52 µg m^{-3} and $SO_{4\,IC}^{2-}$0.78 ± 0.58 µg m^{-3}). The difference between the NO_3^- concentrations in NR-PM$_1$ and PM$_1$ for both seasons could be explained by the loss of ammonium nitrate from the filter due to its dissociation into its gaseous precursors. Good agreement was obtained between the summer average NR-PM$_1$ NH_4^+ and PM$_1$ NH_4^+ (0.80 ± 0.37 µg m^{-3} vs 0.70 ± 0.36 µg m^{-3}) in comparison to those obtained in winter (1.11 ± 0.99 µg m^{-3} vs 0.46 ± 0.35 µg m^{-3}). The seasonal variability in nitrate, which displayed higher concentrations in winter, was related to the thermal instability of ammonium nitrate (Seinfeld and Pandis, 2006). A higher share of Cl$^-$ on NR-PM$_1$ in winter (3 %) indicates the influence of coal combustion used for domestic heating (CHMI, 2019b).

Overall, the average SO_4^{2-} concentration obtained in this study was lower than that measured at the Melpitz rural background site (2.44 µg m^{-3} in summer and 1.66 µg m^{-3} in winter, Poulain et al., 2011) and lower than the values presented in previous studies by Schwarz et al. (2016) conducted at NAOK (PM$_{2.5}$ IC 2.30 µg m^{-3} in summer and 3.86 µg m^{-3} in winter) and by Kubelová et al. (2015) conducted in a Prague urban background site (2.0 µg m^{-3} in summer and 4.4 µg m^{-3} in winter). The average summer NO_3^- concentration was comparable to those measured in Melpitz (0.66 µg m^{-3}), NAOK (PM$_{2.5}$ IC 0.55 µg m^{-3}) and Prague (0.80 µg m^{-3}); however, the winter average concentration was lower than those reported in all three studies (Melpitz: 3.62 µg m^{-3}, NAOK: 2.83 µg m^{-3}, Prague: 5.40 µg m^{-3}). The average organic

https://doi.org/10.5194/acp-2021-516
Preprint. Discussion started: 14 July 2021

concentration was lower in summer but higher in winter than the values recorded in Melpitz (6.89 μg m^{-3} (51%) and 2.08 μg m^{-3} (23%), respectively). The comparison of organic mass (OM) by AMS and OC using an OCEC field analyser is shown in Fig. A4. Turpin and Lim, 2001 recommended OM/OC ratio of 2.1 for non-urban (aged) particles and of 1.6 for urban particles. In this study, the average OM/OC ratio was 2.06 (±0.68) in summer and 1.51 (±0.36) in winter. An average OM_1 and $OC_{2.5}$ of 2.1±1.4 was determined at the Hohenpeissenberg rural site in spring, referring to continental OA (Hock et al., 2002). The higher summer OM/OC ratio could be explained by the presence of more oxidized organic compounds, as the products of photochemical reactions increase the average organic molecular weight per carbon weight (Turpin and Lim, 2001). This result is consistent with the increasing OC/EC ratio observed during summer, when photochemical activity leads to larger secondary organic carbon formation (Mbengue et al., 2018, 2020). Another explanation could be the increased boundary layer height, which enables mixing from higher altitudes and therefore the entrainment of aged, and thus more oxidized, aerosols from long-range transport (Querol et al., 1998). On the other hand, the winter season is characterized by fresh emissions of hydrocarbons owing to the lowered boundary layer height in winter, which does not support the transport of oxidized pollutants within the mixing layer (Schwarz et al., 2008).

Table 2. Basic statistics of the NR-PM_1 and eBC concentrations (median, mean, standard deviation (SD) and average share of species in the total concentration) measured during summer and winter. The values were calculated from five-min-resolution CE-corrected data.

Summer	*Org*	SO_4^{2-}	NO_3^-	NH_4^+	Cl^-	*eBC*
Median (μg m^{-3})	4.32	1.53	0.57	0.75	0.06	0.36
Mean (μg m^{-3})	4.97	1.68	0.67	0.80	0.06	0.40
SD	2.92	0.81	0.38	0.37	0.02	0.20
Average share on NR-PM_1	58 %	22 %	9 %	10 %	1 %	--
Winter						
Median (μg m^{-3})	3.35	0.98	1.67	0.93	0.16	0.84
Mean (μg m^{-3})	4.55	1.36	2.03	1.11	0.18	0.92
SD	4.40	1.38	1.71	0.99	0.09	0.77
Average share on NR-PM_1	50 %	14 %	22 %	11 %	3 %	--

Fig. 2. shows the variations in the particle number and volume and in the sulphate, nitrate and organic size distributions as function of time. In summer, several NPF episodes were recorded (Zíková and Ždímal, 2013; Holubová Šmejkalová et al., 2021); however, accumulation-mode particles were prominent in volume and species mass size distributions. The accumulation mode of SO_4^{2-} does not show a large amount of variation, indicating a regional origin. In contrast, NO_3^- shows dial variations in mass concentrations corresponding to the local photochemical formation of this species (Fig. A5). In winter, the accumulation mode dominated all distributions and was linked to regional and/or long-range transport (see 3.4 Size distribution of NR-PM_1).

https://doi.org/10.5194/acp-2021-516
Preprint. Discussion started: 14 July 2021

Atmospheric Chemistry and Physics
Discussions

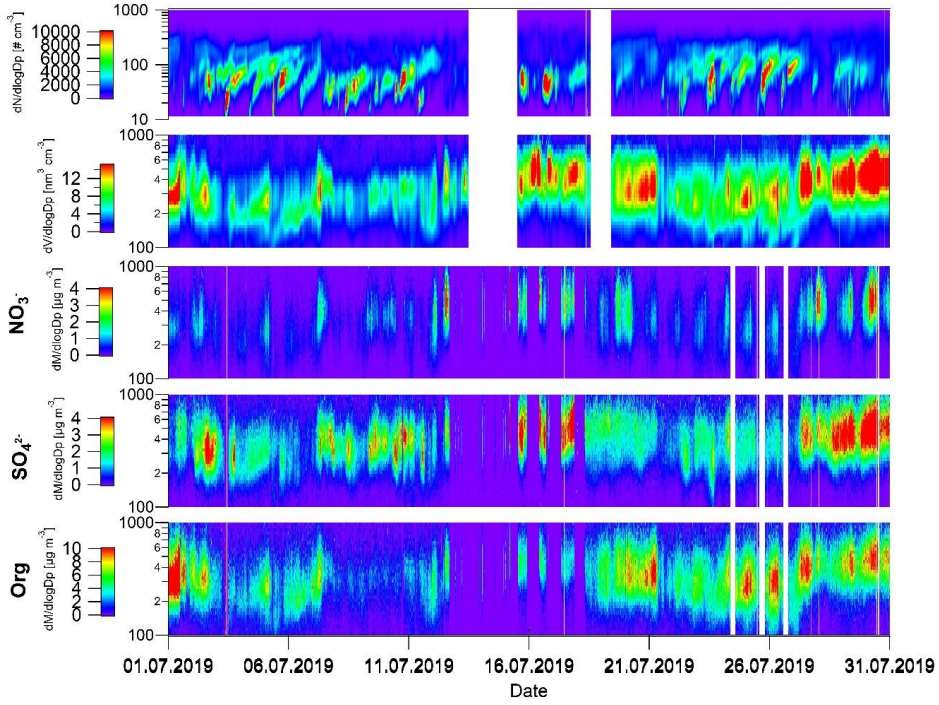

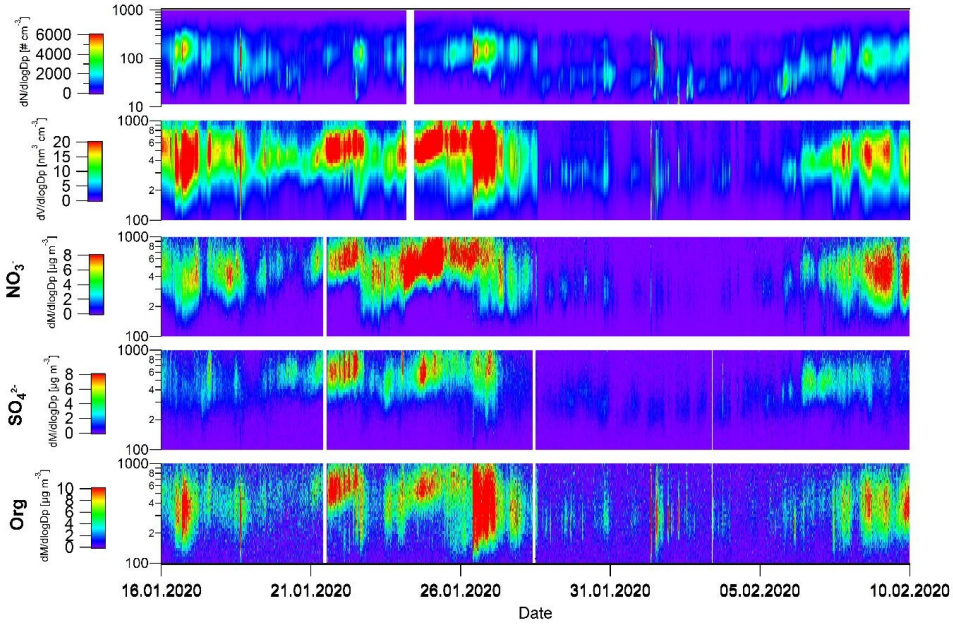

Fig. 2. Time series of particle number and volume concentrations obtained by MPSS (D_{va} recalculated from mobility diameter using a density of 1.50 g cm^{-3}) and mass size distributions of nitrate, sulphate and organics obtained by AMS in summer (top) and in winter (bottom).

https://doi.org/10.5194/acp-2021-516
Preprint. Discussion started: 14 July 2021

Based on the mass size distributions of the species (Fig. 2), ten summer (S1 – 10) and 13 winter (W1 – 13) high-concentration episodes were selected (Table A1). The organic mass dominated in summer; however, distinct episodes of high SO_4^{2-} concentrations (S2, S8, S9, S10) linked to continental air masses from the NW and S-SE were also recorded (Fig. A6). In winter, episodes of dominant SO_4^{2-} (W10) and NO_3^- (W1, W2, W4, W5, W6) concentrations were observed. W10 was influenced by fresh marine air masses reaching NAOK over the UK, Benelux and Germany. The episodes of high NO_3^- concentrations were linked to fresh marine air masses (from the NW) as well as continental air masses (from the NW-SW, Fig. A7).

In summer, the highest Org concentrations (14.58 μg m^{-3}) together with the lowest SO_4^{2-} and NH_4^+ (1.24 μg m^{-3} and 0.91 μg m^{-3}) concentrations were observed during the S1 night-morning episode linked to western continental air masses (Table A1 and Fig. A3). S10 represents the night-morning-early afternoon episode of the highest concentrations of SO_4^{2-}, NO_3^- and NH_4^+ (6.14 μg m^{-3}, 3.37 μg m^{-3}, and 2.98 μg m^{-3}, respectively) resulting from mixed continental air masses (NW-S) that were potentially influenced by emissions from coal power plants situated in North Bohemia.

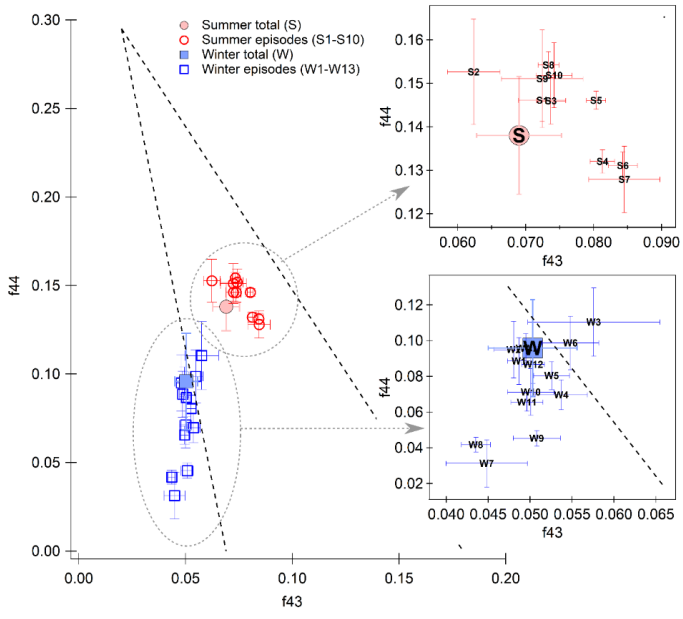

Fig. 3. Comparison of organic fragments f_{44} and f_{43} for the whole summer and winter campaigns (full markers) and for specific episodes (empty markers). Bars represent the standard deviation and the triangular space area typical for ambient OOAs (Ng et al., 2010).

The highest concentrations of Org (15.63 μg m^{-3}) as well as low concentrations of SO_4^{2-}, NO_3^- and NH_4^+ (0.74 μg m^{-3}, 0.93 μg m^{-3} and 0.96 μg m^{-3}, respectively) measured in winter during W7 were influenced by maritime air masses (Fig. A7). Nevertheless, a one-day inversion preceded this episode (Fig. A3), characterized by less oxidized OA (Fig. 3) and $f_{44}f_{60}$ trending towards f_{60} (Fig. A8). In contrast, the highest winter SO_4^{2-} and NH_4^+ concentrations (7.13 μg m^{-3} and 7.90 μg m^{-3}, respectively) measured in the W3 episode and the highest NO_3^-

https://doi.org/10.5194/acp-2021-516
Preprint. Discussion started: 14 July 2021

concentrations (10.66 μg m^{-3}) measured in the W6a episode were characterized by below-freezing temperatures, which probably arose due to inversion conditions in Central Europe.

Organic aerosol ageing was examined on the f_{44} and f_{43} fragments (Fig. 3). Winter aerosols were less oxidized than summer aerosols, pointing to the importance of local sources during the cold part of the year. In summer, the oxidation rate of organic aerosols within the episodes does not differ greatly, and most of the episodes revealed more oxidized organic aerosols (MOOAs) or less volatile organic aerosols (LV-OOAs). Within the summer campaign, the most oxidized aerosols were detected during afternoon episode S2 (Fig. 3), at which time the highest global radiation was also measured (Table A1.). In contrast, S4, S6 and S7 represent night-time and early morning episodes, and S5 represents a night-time and morning episode, and thus less oxidized aerosols (Fig. 3). In winter, the difference between the episodes is more obvious, mainly due to the higher variability in the local sources that influence the receptor site. The W7, W8 and W9 (Fig. 3) episodes are exceptions; these episodes were linked to fresh marine air masses (Fig. A7.).

The f_{60} fragment was used as a biomass-burning (BB) marker. If ambient aerosols are characterized by f_{60} higher than 0.003, they are considered to be influenced by BB emissions (Cubison et al., 2011). During both campaigns, the average f_{60} was 0.003, in contrast to the presence of levoglucosan in the PM_1 samples during both seasons (summer average 0.02 ± 0.02 μg m^{-3} and winter average 0.18 ± 0.20 μg m^{-3}). Levoglucosan concentrations point to BB influence, which was similarly discussed in previous studies conducted at NAOK by Schwarz et al. (2016) and Mbengue et al. (2020). Additionally, a comparison of fragments f_{44} and f_{60} enabled us to assess the presence of fresh organic aerosols emitted by BB (e.g., Milic et al., 2017) revealing that aged organic aerosols from BB influenced the site during both seasons (Fig. A9). The comparison of organic fragments f_{44} and f_{60} determined at the rural and urban background sites shows a difference in the ageing of BB emissions, with the presence of fresh organic aerosols at the urban site and aged organic aerosols at the rural site in winter (Fig. A9).

To determine the origin of NR-PM_1 species, back-trajectories describing their air mass origins were clustered using the HYSPLIT model into 6 and 5 clusters in summer and winter, respectively (Fig. 4.) and linked to the organic, nitrate, sulphate, ammonium and chloride concentrations. A seasonal difference was observed in the air mass back-trajectories, with continental air masses prevailing in summer and marine air masses prevailing in winter.

In summer, cluster #1 (continental air masses from the W-NW, 29%) and cluster #3 (fresh marine air masses from the NW, 28%) were most frequent. Although aged continental air masses from the SE probably related to stable anticyclonic conditions (cluster #6) were rare (7%), they were connected with the highest concentrations of all NR-PM_1 species, especially SO_4^{2-}, NH_4^+ and Cl^-. NO_3^- was linked to fresh marine air masses (cluster #4, 7%), and Org was linked to continental air masses coming from the W-NW (#1 and #5, 29% and 19%, respectively) (Fig. 4.).

In winter, slow continental air masses from the SW cluster #1 (44%) prevailed. The air masses remaining over Central Europe, likely under inversion conditions, were associated with the highest concentrations of all NR-PM_1 species except Cl^- since there was no statistically significant difference among the clusters at the 0.05 level (Fig. 4.). The high pollution loads over Central Europe agree well with the high average mass concentrations of secondary species

https://doi.org/10.5194/acp-2021-516
Preprint. Discussion started: 14 July 2021

during periods when air masses are advected from Central Europe to Paris (Freney et al., 2011, Crippa et al., 2013; Freutel et al., 2013, Freney et al., 2014).

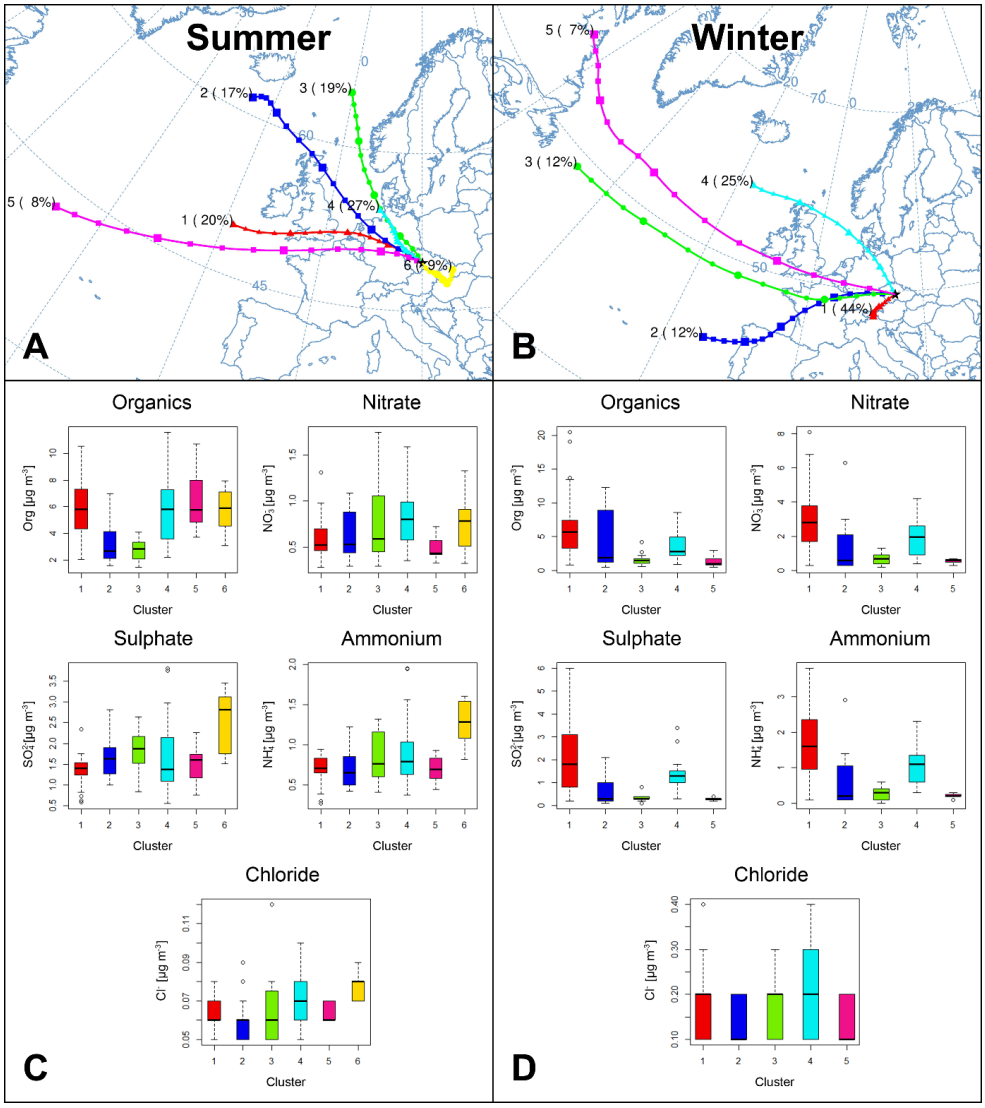

Fig. 4. Geographical locations of the means of the clusters observed in summer (A) and winter (B) along with boxplots of the organic, nitrate, sulphate, ammonium and chloride concentrations in individual clusters measured during the summer (C) and winter (D) campaigns. The boxes are colour coded as the clusters, the black horizontal line is the median, the boxes border the 25th and 75th percentiles and the whiskers represent 1.5 x IQR.

https://doi.org/10.5194/acp-2021-516
Preprint. Discussion started: 14 July 2021

3.4 Size distribution of NR-PM$_1$

The average mass size distributions of the main NR-PM$_1$ species (except chloride) during the entire summer and winter campaign are presented in Table 3. To determine the mode diameters and the widths of the size distributions, the mass distributions were fitted with log-normal modes using the Igor MultiPeak Package as follows:

$$y = M\ exp\left[-\left(\frac{\ln(x/x_0)}{width}\right)^2\right], \qquad (3)$$

where M is the amplitude, x_0 is the peak position in nm, and *width* denotes the peak width. For each season, the mean spectra were fitted separately with one peak, and fitting was also performed for episodes S1-10 and W1-13. Due to the long duration of episode W6, the episode was split into two sections: W6a (67 hours) and W6b (25.5 hours).

The accumulation mode dominated the average mass size distributions during both campaigns, with larger particles of all species observed in winter (Table 3). Shifts towards larger SO_4^{2-}, NO_3^- and NH_4^+ particles in winter compared to summer were also observed in a previous study by Schwarz et al. (2012) that determined urban aerosol chemical compositions and size distributions using a 7-stage impactor with an upstream diffusional aerosol drier. The SO_4^{2-} particles were significantly larger than the NO_3^- particles during both measurement campaigns except for during two episodes (W7 and W9) with regional transport (Table 3). An accumulation mode of $SO_4^{2-}$with regional origin was even detected during a Mexico City Metropolitan Area field study by Salcedo et al. (2006). Dall'Osto et al. (2009) also observed two nitrate particle types at an urban background site, both of which were internally mixed with sulphate, ammonium and carbon: the locally produced particles were smaller than 300 nm , and the regional particles peaked at 600 nm. In a study by Schwarz et al. (2012) at an urban site in Prague, two types of SO_4^{2-} particles were determined. SO_4^{2-} particles in sea-influenced aerosol samples showed maxima between 210 and 330 nm (condensation growth) for both seasons, and SO_4^{2-} particles in continental-influenced samples showed maxima between 500 and 890 nm in winter and between 330 and 500 in summer (droplet-phase growth). NO_3^- particles with maxima between 330 nm and ~500 nm were observed under maritime and continental air masses during both seasons. Freutel et al., 2013 observed a single mode of NR-PM$_1$ species of approximately 300 nm under marine air masses as well as a shift of the accumulation mode to a larger size (approximately 400 nm) during a summer campaign in the Paris region due to aerosol particle ageing of continental air masses from Central Europe. During a summer measurement campaign in New York, the average mass distributions of NO_3^-, $SO_4^{2-}$and NH_4^+ were monomodal, with mode diameters of 440 nm, 450 nm and 400 nm, respectively, and the average Org mass distribution was bimodal, with mode diameters of 80 nm and 360 nm (Drewnick et al., 2004). A study by Freney et al. (2011) conducted during three seasons at the Puy-de-Dôme research station presented a major accumulation mode of NR-PM$_1$ species peaking at 600 nm, indicating aged aerosol particles.

https://doi.org/10.5194/acp-2021-516
Preprint. Discussion started: 14 July 2021

Table 3. Average size distributions of species measured by AMS (D_p corresponds to the vacuum aerodynamic diameter (D_{va})) for the summer (left) and winter (right) campaigns.

	Org	SO_4^{2-}	NO_3^-	NH_4^+
Summer D_{va} (nm)	334	377	401	497
Winter D_{va} (nm)	413	501	547	517

In summer, the smallest mode diameters of Org (279 nm) and NO_3^- (253 nm) were observed during the S7 episode, while for SO_4^{2-} and NH_4^+ (325 nm and 335 nm, respectively), they were influenced by continental air masses of regional origin during the S2 episode (from the N-NE-E, Fig. A6). In contrast, the largest mode diameters (Org: 466 nm, NO_3^-: 491 mm, SO_4^{2-}: 494 nm and NH_4^+: 478 nm) were recorded during the S10 episode by continental long-range transport from the W-NW (Fig. A6). The smallest mode diameters of all species (Org: 295 nm, NO_3^-: 240 nm, SO_4^{2-}: 242 nm and NH_4^+: 365 nm) in winter (W8) were linked to fresh marine air masses, and the largest winter diameters (Org: 563 nm, NO_3^-: 609 nm, SO_4^{2-}: 636 nm and NH_4^+: 607 nm, W3) were linked to the regional and long-range transport of air masses of continental origin and were also probably influenced by inversion conditions (Fig. A7). Additionally, as expected, the Org particle size showed growth, and the increasing mode diameter was more significant in the winter season, with the ageing of aerosols resulting in oxygenated organic aerosols (Fig. 5).

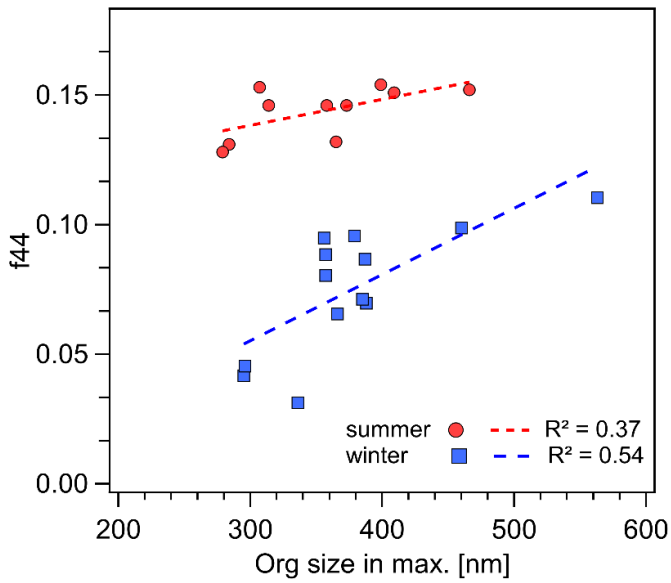

Fig. 5. Relationship between organic fragment f_{44} and the size of the organic fraction during episodes of high NR-PM_1 species mass concentrations in both seasons.

https://doi.org/10.5194/acp-2021-516
Preprint. Discussion started: 14 July 2021

3.5 Particle effective density

The particle effective density was calculated for each episode of high particle numbers and mass concentrations. The episodes were determined as follows: i) PMF application to PNSDs and ii) depiction of mass size distributions of NR-PM_1 species in a 3D plot (Fig. 2).

The PMF model was run several times until the most physically meaningful results and the best diagnostics were obtained. The two-sided size bins containing variables (9.7 nm, 11.5 nm, 557.2 nm and 733.6 nm; midpoint of the size bins) were set as weak along with the total variables (N10 – 800). The model was run with different factor numbers (3 – 8). The most stable solution was found when 6 factors in summer and 5 factors in winter were considered (Fig. A10). With all runs converged, the scaled residuals were normally distributed, any unmapped factors were detected with bootstrap error estimations. No swaps were observed with the displacement error analysis, indicating that the solution was stable (Table A2). The non-normalized PNSD (N cm^{-3}) was analysed using the model.

3.5.1 Episodes of high particle number concentrations

One high-particle-contribution episode occurred in summer, and eight short episodes occurred in winter ($W1_{MPSS}$, factor 3 of 5 and $W2_{MPSS}$ – $W8_{MPSS}$, factor 1 of 5; the durations ranged from 25 to 95 minutes). No NR-PM_1 data were available for effective density calculations during the summer period (3rd July from 9:20 to 10:05). The effective density ranged between 1.40 and 1.85 g cm^{-3} (Table 4). During $W1_{MPSS}$, accumulation-mode particles dominated (F3, mode diameter ~429 nm, Fig. A10) with an effective density of 1.85 g cm^{-3}. A density of 1.85 g cm^{-3} corresponds to black carbon (Martins et al., 1998), and a density of 2.0 g cm^{-3} relates to aged biomass-burning particles (Moffet et al., 2008). The remaining episodes ($W2_{MPSS}$ – $W8_{MPSS}$) were linked mainly to particles of the Aitken mode (F1, mode diameter ~32 nm, Fig. A10) with effective densities ranging from 1.40 to 1.60 g cm^{-3}. Rissler et al. (2014) observed the dominance of particles with effective density ~ 1.4 g cm^{-3} at a rural background site (Vavihill, Sweden) during the winter months, and Qiao et al. (2018) reported a decrease in particle effective densities ranging from 1.43 to 1.55 g cm^{-3} at rural sites (Changping, China) with increasing particle sizes.

Table 4. Particle effective densities (g cm^{-3}) calculated during episodes of high particle contributions to N10 – 800 using MPSS data.

Episode MPSS	**W1**	**W2**	**W3**	**W4**	**W5**	**W6**	**W7**	**W8**
Density	1.85	1.45	1.50	1.55	1.45	1.55	1.40	1.60
# of spectra	13	8	8	19	7	5	8	8

3.5.2 Episodes of high mass concentrations

The densities calculated based on the particle mass size distributions using Eq. (1) corresponding to the episodes discussed in section 3.4 (Size distribution of NR-PM_1) ranged from 1.40 – 1.60 g cm^{-3} in summer and from 1.30 – 1.75 g cm^{-3} in winter (Table 5, Fig. A11 and Fig. A12). In comparison, the densities calculated using Eq. (2) were lower in both seasons, ranging from 1.30 to 1.40 g cm^{-3} in summer (with a seasonal average of 1.34 ± 0.28 g cm^{-3}) and from 1.30 to 1.50 g cm^{-3} in winter (with a seasonal average of 1.44 ± 0.16 g cm^{-3}) (Table 5).

https://doi.org/10.5194/acp-2021-516
Preprint. Discussion started: 14 July 2021

The average summer density did not show a diurnal trend compared to the winter density (Fig. A13), followed by a diurnal trend (inverse dependence) observed for organics (Fig. A5). The summer diurnal variation in the concentrations of organics was flatter than that in winter and was not sufficient to significantly affect the diurnal density trend. In summer, we observed the most significant diurnal trend for nitrate, but the absolute concentrations of nitrate were low, and this variation therefore did not significantly affect the summer diurnal density trend (Fig. A5).

In summer, with a higher ratio of ammonium sulphate, the density increased. In winter, the density was influenced by the inorganic content (ammonium nitrate and sulphate). In both seasons, the density increased with a decrease in the organic ratio and vice versa. This relation evidently arises from the parameters in Eq. (2) (Fig. A14). The largest uncertainty in the PM density calculations performed using Eq. (2) is linked to the density of organics, which was set to 1.2 g cm^{-3}. The density applied for the organic fraction refers to the urban and urban background stations (Turpin and Lim, 2001), and the organics density of a rural background site is expected to be higher than that of an urban site due to organic aerosol ageing. However, a density of 1.2 g cm^{-3} was also utilized in a study conducted by Freney et al. (2011) at a mid-altitude Puy-de-Dôme site and in a study conducted by Poulain et al. (2020) at a rural background site in Melpitz. In this study, as the mass fraction of organics in the aerosols increased, the density calculated using Eq. (2) converged to a value of 1.2 g cm^{-3} (Fig. A14).

Table 5. Particle effective densities (g cm^{-3}) calculated during episodes of high mass concentrations using AMS data.

Episode AMS	**S1**	**S2**	**S3**	**S4**	**S5**	**S6**	**S7**	**S8**	**S9**	**S10**
Density*	1.45	1.60	1.50	1.55	1.40	1.45	1.45	1.45	1.45	1.50
Density**	1.30	1.40	1.40	1.40	1.30	1.30	1.30	1.35	1.40	1.40
# of spectra	145	61	73	61	49	109	109	133	265	169

Episode AMS	**W1**	**W2**	**W3**	**W4**	**W5**	**W6a**	**W6b**	**W7**	**W8**	**W9**	**W10**	**W11**	**W12**	**W13**
Density*	1.40	1.40	1.70	1.60	1.70	1.6	1.55	1.55	1.60	1.45	1.75	1.50	1.60	1.55
Density**	1.40	1.50	1.50	1.50	1.50	1.50	1.40	1.30	1.30	1.30	1.50	1.40	1.40	1.40
# of spectra	175	229	337	85	25	805	307	19	25	19	97	115	31	139

* Density calculated using Eq. 1.
** Density calculated using Eq. 2 (Salcedo et al., 2006).

The differences between the densities obtained using the two approaches (spectra fitting – Eq. 1 versus chemical equation – Eq. 2.), ranging from 2 – 12% in summer and 7 – 19% in winter, indicate the presence of different compounds of lower or higher densities that are not taken into consideration by the effective density calculations, as well as the lower density used for organics in Eq. (2), the physical characteristics of the particles, such as the particle size, porosity and non-compactness, and calculation uncertainties that are primarily related to the single CE correction used for the whole data set. The smaller differences between the two approaches obtained in summer indicate aerosol particles composed mainly of NR-PM_1 species along with

https://doi.org/10.5194/acp-2021-516
Preprint. Discussion started: 14 July 2021

eBC. In winter, the differences were larger, and both negative (compounds with lower densities and/or particle physical characteristics) and positive (compounds with higher densities) differences were obtained. However, the larger differences in winter could be strongly influenced by the considerable CE correction applied to the AMS data.

4. Summary and conclusions

This study is the first of its kind in the Czech Republic, assessing the seasonal variability of NR-PM_1 based on its chemically speciated mass size distribution, density, and origin at a rural background site. The impacts of atmospheric regional and long-range transport in Central Europe were examined based on intensive measurement campaigns conducted at National Atmospheric Observatory Košetice (NAOK) in summer 2019 and winter 2020.

The CE correction performed based on comparisons between sulphate concentrations measured by AMS and IC was applied to the NR-PM_1 data (0.4 in summer and 0.33 in winter), resulting in very good agreement between the AMS and MPSS volume and mass concentration in summer (slope=1.08, R^2=0.96 and slope=1.00, R2=0.97, respectively) and winter (slope=0.93, R^2=0.94 and slope=0.89, R^2=0.94, respectively). Near-real-time and systematic comparisons with reference methods represent the best way to obtain quality assurance of the AMS data and are needed to better characterize the robustness of the AMS data over long sampling time (Poulain et al., 2020).

The average NR-PM_1+eBC concentrations were 8.58±3.70 μg m^{-3} in summer and 10.08±8.04 μg m^{-3} in winter, with organics dominating during both seasons, followed by SO_4^{2-} in summer and NO_3^- in winter. The different seasonal compositions in PM_1 were caused by different sources and variable properties of individual compounds and were related to different meteorological conditions during these two seasons in the Czech Republic, as was previously mentioned by Kubelová et al., 2015.

The accumulation mode dominated the average mass size distributions during both seasons, with larger particles of all species in winter linked to seasonally differentiated regional and long-range origins as well as to the variability in the local sources primarily observed in winter. Although summer-aged continental air masses from the SE were rare (7%), they were connected to the highest concentrations of all NR-PM_1 species. In winter, the slow continental air masses from the SW (44 %) linked to inversion conditions over Central Europe were associated with the highest concentrations of organics, sulphate, nitrate, and ammonium.

The application of PMF on the PNSD enabled us to distinguish eight episodes of high particle contributions to N10-800 to calculate the particle effective density based on the particle number and mass size distributions. Additionally, a comparison of spectra fitting and chemical-based calculations for determining the particle effective density during episodes of high mass concentrations revealed differences in these two approaches due to the presence of compounds that were not taken into consideration by the density calculations, such as particle physical characteristics and calculation uncertainties.

Data availability.

All relevant data for this paper are archived at the ICPF of the CAS (Institute of Chemical Process Fundamentals of the Czech Academy of Sciences) and are available upon request from the corresponding author (Petra Pokorná).

https://doi.org/10.5194/acp-2021-516
Preprint. Discussion started: 14 July 2021

Author contribution.

PP, JS and VŽ conceived the research. PP, RL, PV, SM, AHŠ and JO conducted the atmospheric aerosol measurements during both intensive campaigns. PP, NZ, RL, PV, VR and JS analysed and interpreted the data. PP prepared the manuscript with contributions from all co-authors.

Competing interests

The authors declare that they have no conflict of interest.

Acknowledgements

We would like to thank Daniel Vondrák for the graphical editing. Thanks also goes to American Journal Experts for the English proof reading of the manuscript. The authors gratefully acknowledge the NOAA Air Resources Laboratory (ARL) for the provision of the HYSPLIT transport and dispersion model and/or READY website (http://www.ready.noaa.gov) used in this publication. We greatly thank the two anonymous reviewers for their effort to critically review the manuscript and for providing constructive comments.

Financial support

This work was supported by the GACR under grant P209/19/06110Y and by the MEYS of the Czech Republic under grant ACTRIS-CZ LM2018122 and ACTRIS-CZ RI (CZ.02.1.01/0.0/0.0/16_013/0001315) as well as by COST Action CA16109 COLOSSAL within STSM.

References

Allan, J.D., Delia, A.E., Coe, H., Bower, K.N., Alfarra, M.R., Jimenez, J.L., Middlebrook, A.M., Drewnick, F., Onasch, T.B., Canagaratna, M.R., Jayne, J.T., Worsnop, D.R., 2004. A generalised method for the extraction of chemically resolved mass spectra from Aerodyne aerosol mass spectrometer data. J. Aerosol Sci. 35, 909–922.

Allan, J.D., Alfarra, M.R., Bower, K.N., Coe, H., Jayene, J.T., Worsnop, D.R., Aalto, P.P., Kulmala, M., Hyötyläinen, T., Cavalli, F., Laaksonen, A., 2006. Size and composition measurements of background aerosol and new particle growth in a Finnish forest during QUEST 2 using an Aerodyne Aerosol Mass Spectrometer. Atmos. Chem. Phys. 6, 315–327.

Belis, C.A., Karagulian, F., Larsen, B.R., Hopke, P.K., 2013. Critical review and metaanalysis of ambient particulate matter source apportionment using receptor models in Europe. Atmos. Environ. 69, 94–108.

Bressi, M., Cavalli, F., Putaud, J.P., Fröhlich, R., Petit, J.-E., Aas, W., Äijälä, A., Alastuey, A., Allan, J.D., Aurela, M., Berico, M., Bougiatioti, A., others. 2021. A European aerosol phenomenology - 7: High-time resolution chemical characteristics of submicron particulate matter across Europe. Atmospheric Environmnet: X 10, 100108, 1–16.

Carslaw, D.C., Ropkins, K., 2012. Openair – an R package for air quality data analysis. Environ. Model. Software 27–28, 52–61.

Cavalli, F., Viana, M., Ytri, K.E., Genberg, J., Putaud, J.-P., 2010. Toward a standardised thermal-optical protocol for measuring atmospheric organic and elemental carbon: the EUSAAR protocol. Atmospheric Measurement Techniques 3, 79–89.

https://doi.org/10.5194/acp-2021-516
Preprint. Discussion started: 14 July 2021

Costabile, F., Birmili, W., Klose, S., Tuch, T., Wehner, B., Wiedensohler, A., Franck, U., König, K. and Sonntag, A., 2009. Spatio-Temporal Variability and Principal Components of the Particle Number Size Distribution in an Urban Atmosphere. Atmos. Chem. Phys. 9: 3163–3195.

CHMI, Tabular Survey 2019, Czech Hydrometeorological Institute (CHMI) 2019(a) http://portal.chmi.cz/files/portal/docs/uoco/isko/tab_roc/2019_enh/index_GB.html, last access: 4.6.2021

CHMI, Annual report 2019, Czech Hydrometeorological Institute (CHMI) 2019(b) https://www.chmi.cz/files/portal/docs/uoco/isko/grafroc/19groc/gr19cz/19_rocenka_UKO_web_tisk_up1.pdf, last access: 4.6.2021

Cubison, M.J., Ortega, A.M., Hayes, P.L., Farmer, D.K., Day, D., Lechner, M.J., Brune, W.H., Apel, E., Diskin, G.S., Fisher, J. a., Fuelberg, H.E., Hecobian, A., Knapp, D.J., Mikoviny, T., Riemer, D., Sachse, G.W., Sessions, W., Weber, R.J., Weinheimer, A.J., Wisthaler, A., Jimenez, J.L., 2011. Effects of aging on organic aerosol from open biomass burning smoke in aircraft and laboratory studies. Atmos. Chem. Phys. 11, 12049–12064.

Dall'Osto , M., Harrison, R.M., Coe, H., Williams, P.I., Allan, J.D., 2009. Real time chemical characterization of local and regional nitrate aerosols. Atmos. Chem. Phys., 9, 3709-3720.

DeCarlo, P.F., Slowik, J.G., Worsnop, D.R., Davidovits, P., Jimenez, J.L., 2004. Particle Morphology and Density Characterization by Combined Mobility and Aerodynamic Diameter Measurements. Part 1: Theory. Aerosol Sci. Technol. 38, 1185–1205.

Drewnick, F., Jayne, J.T., Canargaratna, M., Worsnop, D.R., Demerjian, K.L., 2004. Measurement of ambient aerosol composition during the PMTACS-NY 2001 Using and Aersosol Mass Spectrometer. Part II: Chemically speciated mass distribution.

Drewnick, F., Hings, S.S., DeCarlo, P., Jayne, J.T., Gonin, M., Fuhrer, K., Weimer, S., JImenez, J.L., Demerjian, K.L., Borrmann, S., Worsnop, R., 2005. A new Time-of-Flight Aerosol Mass Spectrometer (TOF-AMS) – Instrument description and first field deployment. Aerosol Science and Technology 39, 637–658.

EEA, 2019. Air Quality in Europe - 2019 Report. European Environment Agency Report No 10/2019. https://www.eea.europa.eu/publications/air-quality-in-europe-2019.

Freney, E. J., Sellegri, K., Canonaco, F., Boulon, J., Hervo, M., Weigel, R., Pichon, J. M., Colomb, A., Prévôt, A.S.H., and Laj, P., 2011. Seasonal variations in aerosol particle composition at the puy-de-Dôme research station in France, Atmos. Chem. Phys., 11, 13047–13059.

Freney, E.J., Sellegri, K., Canonaco, F., Colomb, A., Borbon, A., Michoud, V., Doussin, J.,F., Crumeyrolle, S., Amarouche, N., Pichon, J.M., Bourianne, L., Gomes, L., Prévôt, A.S.H., Beekmann, M., Schwarzenböeck, A., 2014. Characterizing the impact of urban emission on regional aerosol particles: airborne measurements during the MEGAPOLI experiment. Atmos. Chem. Phys. 14, 1397–1412.

Freutel., F., Schneider, J., Drewnick, von der Weiden-Reinmüller, S.L., Crippa, M., Prévôt, A.S.H., Baltensprenger, U., Poulain, L., Wiedensohler, A., Sciare, J., Sarda-Esteve, R., Burkhart, J.F., Eckhardt, S., Stohl, A., Gros, V., Colomb, A., Michoud, V., Doussin, J.F., Borbon, A., Haeffelin, M., Morille, Y., Beekmann, M., Borrmann, S., 2013. Aeosol particle measurements at three stationary sites in the megacity of Paris during summer 2009: meteorology and air mass origin dominated aerosol particle composition and size distribution. Atmos. Chem. Phys. 13, 933–959.

Fröhlich, R., Cubison, M. J., Slowik, J. G., Bukowiecki, N., Canonaco, F., Croteau, P. L., Gysel, M., Henne, S., Herrmann, E., Jayne, J. T., Steinbacher, M., Worsnop, D. R., Baltensperger, U., and Prévôt, A. S. H., 2015. Fourteen months of on-line measurements of the non-refractory submicron aerosol at the Jungfraujoch (3580 m a.s.l.) – chemical composition, origins and organic aerosol sources. Atmos. Chem. Phys. 15, 11373–11398.

https://doi.org/10.5194/acp-2021-516
Preprint. Discussion started: 14 July 2021

Hersey, S.P., Craven, J.S., Shilling, K.A., Metcalf, A.R., Sorooshian, A., Chan, M.N., Flagan, R.C., Seinfeld, J.H., 2011. The Pasadena Aerosol Characterization Observatory (PACO): chemical and physical analysis of the Western Los Angeles basin aerosol. Atmos. Chem. Phys. 11, 7417–7443.

Holubová Šmejkalová, A., Zíková, N., Ždímal, V., Plachá, H., Bitter, M., 2021. Atmospheric aerosol growth rates at different background station types. Environmental Science and Pollution Research 28, 13352–13364.

Hock, N., Schneider, J., Borrmann, S., Römpp, A., Moortgat, G., Franze, T., Schauer, C., Pöschl, U., Plass-Dülmer, C., Berresheim, H., 2008. Rural continental aerosol properties and processes observed during the Hohenpeissenberg Aerosol Characterization Experiment (HAZE2002). Atmos. Chem. Phys. 8, 603–623.

Hu, M., Peng, J., Sun, K., Yue, D., Guo, S., Wiedensohler, A., Wu, Z., 2012. Estimation of size-sesolved smbient particle density based on the measurement of aerosol number, mass, and chemical Size Distributions in the winter in Beijing. Environmental Science & Technology 46, 9941−9947.

Jayne, J. T., Leard, D. C., Zhang, X., Davidovits, P., Smith, K. A., Kolb, C. E., and Worsnop, D. R., 2000. Development of an Aerosol Mass Spectrometer for Size and Composition Analysis of Submicron Particles, Aerosol Sci. Technol., 33, 49–70, 2000.

Jimenez, J. L., Jayne, J. T., Shi, Q., Kolb, C. E., Worsnop, D. R., Yourshaw, I., Seinfeld, J. H., Flagan, R. C., Zhang, X., Smith, K. A., Morris, J., and Davidovits, P., 2003. Ambient aerosol sampling using the Aerodyne Aerosol Mass Spectrometer, J. Geophys. Res., 108, 8425.

Kozáková, J., Pokorná, P., Vodička, P., Ondráčková, L., Ondráček, J., Křůmal, K., Mikuška, P., Hovorka, J., Moravec, P., Schwarz, J., 2019. Influence of regional air pollution transport at a European air pollution hotspot. Environ Sci Pollut Res 26, 1675–1692.

Křůmal., K., Mikuška, P., 2020. Mass concentrations and lung cancer risk assessment of PAHs bound to PM1 aerosol in six industrial, urban and rural areas in the Czech Republic, Central Europe. Atmospheric Pollution Research 11, 401–408.

Kubelová, L., Vodička, P., Schwarz, J., Cusack, M., Makeš, O., Ondráček, J., Ždímal, V., 2015. A study of summer and winter high time-resolved submicron aerosol composition measured at a suburban site in Prague. Atmospheric Environment 118, 45–57.

Leoni, C., Pokorná, P., Hovorka, J., Masiol, M., Topinka, J., Zhao, Y., Křůmal, K., Cliff, S., Mbengue, S., Fusek, M., Schwarz, J., Vodička, P., Holubová Šmejkalová, A. Holoubek, I., 2018. Four years of highly time resolved measurements of elemental and organic carbon at a rural background site in Central Europe. Atmos. Environ., 182, 335–346.

Lide, D. R.: CRC Handbook of Chemistry and Physics, CRC Press Inc, USA, 1991.

Mbengue, S., Serfozo, N., Schwarz, J., Ziková, N., Holubová Šmejkalová, A., Holoubek, I. 2020. Characterization of Equivalent Black Carbon at a regional background site in Central Europe: Variability and source apportionment. Environmental Pollution 260, 113771

Mikuška, P., Hopke, P.K., 2018. Source apportionment of aerosol particles at a European air pollution hot spot using particle number size distributions and chemical composition. Environ. Pollut. 234, 145–154.

Martins, J.V., Artaxo, P., Liousse, C., Reid, J.S., Hobbs, P.V., Kaufman, Y.J., 1998. Effects of black carbon content, particle size, and mixing on light absorption by aerosols from biomass burning in Brazil. Journal of Geophysical Research 103, 32,041-32,050.

Middlebrook, A.M., Bahreini, R., Jimenez, J.L., Canagaratna, M.R., 2012. Evaluation of Composition-Dependent Collection Efficiencies for the Aerodyne Aerosol Mass Spectrometer using Field Data. Aerosol Science and Technology 46, 258–271.

Milic, A., Mallet, M.D., Cravigan, L.T., Alroe, J., Ristovski, Z.D., Selleck, P., Lawson, S.J., Ward, J., Desservettaz, M.J., Paton-Walsh, C., Williams, L.R., Keywood, M.D., Miljevic,

https://doi.org/10.5194/acp-2021-516
Preprint. Discussion started: 14 July 2021

B., Biomass burning and biogenic aerosols in northern Australia during the SAFIRED campaign. Atmos. Chem. Phys. 17, 3945–3961.

Moffet, R. C., Qin, X. Y., Rebotier, T., Furutani, H., and Prather, K. A., 2008. Chemically segregated optical and microphysical properties of ambient aerosols measured in a single-particle mass spectrometer, J. Geophys. Res.-Atmos., 113, D12213.

Ng, N.L., Canagaratna, M.R., Zhang, Q., Jimenez, J.L., Tian, J., Ulbrich, I.M., Kroll, J.H., Docherty, K.S., Chhabra, P.S., Bahreini, R., Murphy, S.M., Seinfeld, J.H., Hildebrandt, L., Donahue, N.M., DeCarlo, P.F., Lanz, V.A., Prévot, A.S.H., Dinar, E., Rudich, Y., Worsnop, D.R., 2010. Organic aerosol components observed in Northern Hemispheric datasets from Aerosol Mass Spectrometry. Atmos. Chem. Phys. 10, 4625–4641.

Park, K., Kittelson, D. B., Zachariah, M. R., and McMurry, P. H.: Measurement of Inherent Material Density of Nanoparticle Agglomerates, J. Nanopart. Res., 6, 267–272, 2004.

Pitz, M., Cyrys, J., Karg, E., Wiedensohler, A., Wichmann, H.E.,Heinrich, J., 2003. Variability of apparent particle density of an urban aerosol. Environmental Science & Technology 37, 4336-4342.

Pitz, M., Schmid, O., Heinrich, J., Birmili, W., Maguhn, J., Zimmermann, R., Wichmann, H.E., Peters, A., Cyrys, J., 2008. Seasonal and Diurnal Variation of $PM_{2.5}$ Apparent Particle Density in Urban Air in Augsburg, Germany. Environmental Science & Technology 42, 5087–5093.

Pokorná, P., Schwarz, J., Krejci, R., Swietlicki, E., Havránek, V., Ždímal, V., 2018. Comparison of PM2.5 chemical composition and sources at a rural background site in Central Europe between the years 1993/1994/1995 and 2009/2010: Effect of legislative regulations and economic transformation on the air quality. Environmental Pollution 241, 841-851.

Poulain, L., Spindler, G., Birmili, W., Plass-Dülmer, C., Wiedensohler, A., Herrmann, H., 2011. Seasonal and diurnal variations of particulate nitrate and organic matter at the IfT research station Melpitz. Atmos. Chem. Phys. 11 (24), 12579–12599.

Poulain, L., Spindler, G., Grüner, A., Tuch, T., Stieger, B., van Pinxteren, D., Petit, J.-E., Favez, O., Herrmann, H., Wiedensohler, A., 2020. Multi-year ACSM measurements at the central European Research station Melpitz (Germany) – Part 1: Instrument robustness, quality assurance, and impact of upper size cutoff diameterAtmos. Meas. Tech., 13, 4973–4994.

Putaud, J.P., Raes, F., Van Dingenen, R., Brüggemann, E., Facchini, M., Decesari, S.,Fuzzi, S., Gehrig, R., Hüglin, C., Laj, P., others, 2004. A European aerosol phenomenology—2: chemical characteristics of particulate matter at kerbside, urban, rural and background sites in Europe. Atmos. Environ. 38, 2579–2595.

Putaud, J.P., Van Dingenen, R., Alastuey, A., Bauer, H., Birmili, W., Cyrys, J., Flentje, H., Fuzzi, S., Gehrig, R., Hansson, H.C., others, 2010. A European aerosol phenomenology — 3: physical and chemical characteristics of particulate matter from 60 rural, urban, and kerbside sites across Europe Atmos. Environ. 44, 1308–1320.

Qiao, K., Wu, Z., Pei, X., Liu, Q., Shang, D., Zheng, J., Du, Z., Zhu, W., Wu, Y., Lou, S., Guo, S., Chan, C.K., Pathak, R.K., Hallquist, M., Hu, M., 2018. Size-resolved effective density of submicron particles during summertime in the rural atmosphere of Beijing, China. Journal of Environmental Sciences 73, 69–77.

Querol, X., Alastuey, A., Puicercus, J.A., Mantilla, E., Ruiz, C.R., Lopez-Soler, A., Plana, F., Juan, R., 1998. Seasonal evolution of suspended particles around a large coal-fired power station: chemical characterization. Atmos. Environ. 32, 719-731.

Rissler, J., Nordin, E.Z., Eriksson, A.C., Nilsson, P.T., Frosch, M., Sporre, M.K., Wierzbicka, A., Svenningsson, B., Löndahl, J., Messing, M.E., Sjogren, S., Hemmingsen, J.G., Loft, S., Pagels, J.H., Swietlicki, E., 2014. Environ. Sci. Technol. 48, 11, 6300–6308

https://doi.org/10.5194/acp-2021-516
Preprint. Discussion started: 14 July 2021

Rolph, G., Stein, A., Stunder, B., 2017. Real-time environmental applications and display sYstem: READY. Environ. Model. Software 95, 210–228.

Salcedo, D., Onasch, T. B., Dzepina, K., Canagaratna, M. R., Zhang, Q., Huffman, J. A., DeCarlo, P. F., Jayne, J. T., Mortimer, P., Worsnop, D. R., Kolb, C. E., Johnson, K. S., Zuberi, B., Marr, L. C., Volkamer, R., Molina, L. T., Molina, M. J., Cardenas, B., Bernabé, R. M., Márquez, C., Gaffney, J. S., Marley, N. A., Laskin, A., Shutthanandan, V., Xie, Y., Brune,W., Lesher, R., Shirley, T., and Jimenez, J. L., 2006. Characterization of ambient aerosols in Mexico City during the MCMA-2003 campaign with Aerosol Mass Spectrometry: results from the CENICA Supersite. Atmos. Chem. Phys. 6, 925–946.

Salimi, F., Crilley, L.R., Stevanovic, S., Ristovski, Z., Mazaheri, M., He, C., Johnson, G., Ayoko, G., Morawska, L., 2015. Insights into the growth of newly formed particles in a subtropical urban environment. Atmos. Chem. Phys. 15, 13475–13485.

Schwarz, J., Chi, X., Maenhaut, W., Civis, M., Hovorka, J., Smolík, J., 2008. Elemental and organic carbon in atmospheric aerosols at downtown and suburban sites in Prague. Atmos. Res. 90, 287-302.

Schwarz, J., Štefancová, L., Maenhaut, W., Smolík, J., Ždímal, V., 2012. Mass and chemically speciated size distribution of Prague aerosol using an aerosol dryer – The influence of air mass origin. Science of the Total Environment

Schwarz, J., Cusack, M., Karban, J., Chalupníčková, E., Havránek, V., Smolk., J., Ždímal., V., 2016. $PM_{2.5}$ chemical composition at a rural background site in Central Europe, including correlation and air mass back trajectory analysis. Atmospheric Research 176–177, 108–20.

Seinfeld, J.H., Pandis, S.N., 2006. Atmospheric Chemistry and Physics. John Wiley & Sons, New York.

Turpin, B. J. and Lim, H.-J., 2001. Species contributions to PM2.5 mass concentrations: revisiting common assumptions for estimating organic mass, Aerosol Sci. Tech., 35, 302–610.

Vodička, P., Kawamura, K., Schwarz, J., Kunwar, B., Zdimal, V., 2019. Seasonal study of stable carbon and nitrogen isotopic composition in fine aerosols at a Central European rural background station. Atmos. Chem. Phys. 19, 3463–3479.

Vu, T.V., Delgado-Saborit, J.M., Harrison, R.M., 2015. Review: particle number size distributions from seven major sources and implications for source apportionment studies. Atmos. Environ. 122, 114–132.

Watson, J.G., Chow J.C., 2011, Ambient aerosol sampling. In: Kulkarni, P, Baron, P.A, Willeke, K (eds) Aerosol measurement: principles, techniques and applications, third edition, 3rd edn. John Wiley & Sons, Inc., Hoboken, NJ, USA, pp 591–614.

Wickham, H., 2016. ggplot2: Elegant Graphics for Data Analysis. Springer-Verlag, New York.

Zíková, N., Ždímal, V., 2013. Long-Term Measurement of Aerosol Number Size Distributions at Rural Background Station Košetice. Aerosol and Air Quality Research, 13, 1464–1474.

Zíková, N., Ždímal, V., 2016. Precipitation scavenging of aerosol particles at a rural site in the Czech Republic. Tellus B: Chemical and Physical Meteorology 68, 27343, 1–14.

https://doi.org/10.5194/acp-2021-516
Preprint. Discussion started: 14 July 2021

APPENDIX

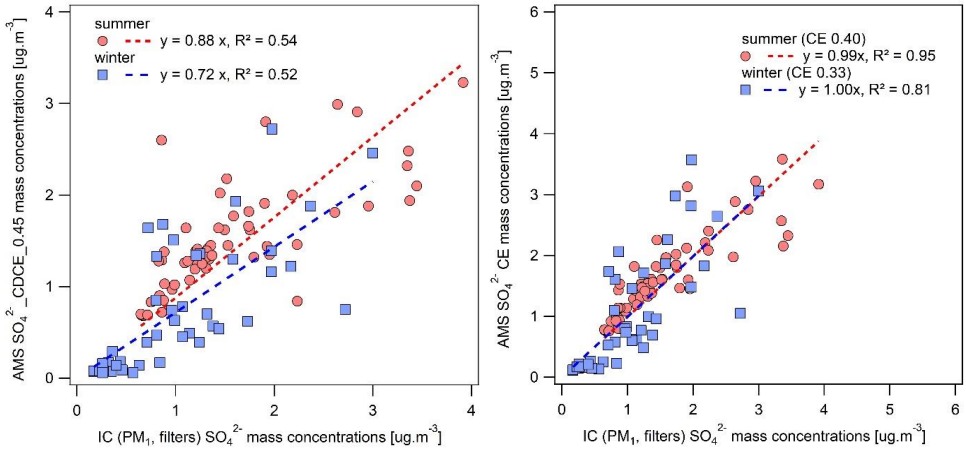

Figure A1. Comparison of sulphate concentration measured by AMS and retrieved from PM_1 filter analysis by IC with applied CDCE correction (left) and constant CE correction (right) for both measurement seasons.

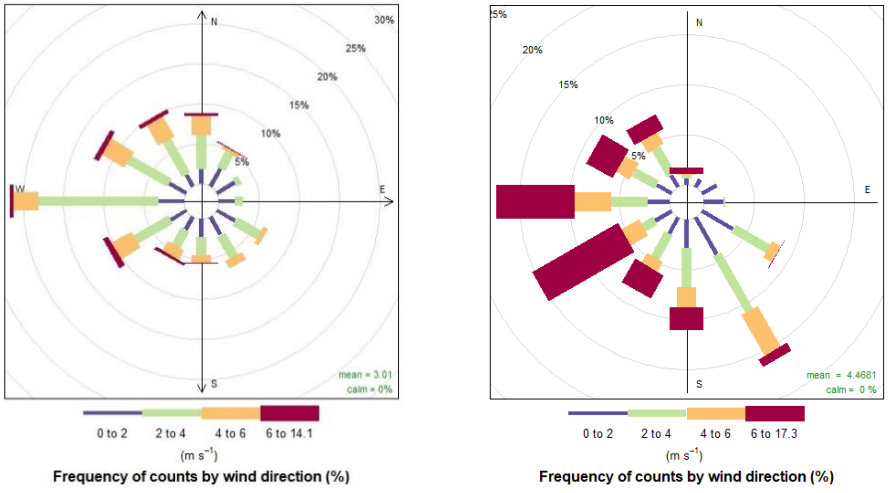

Figure A2. Wind rose summer (left) and winter (right).

https://doi.org/10.5194/acp-2021-516
Preprint. Discussion started: 14 July 2021

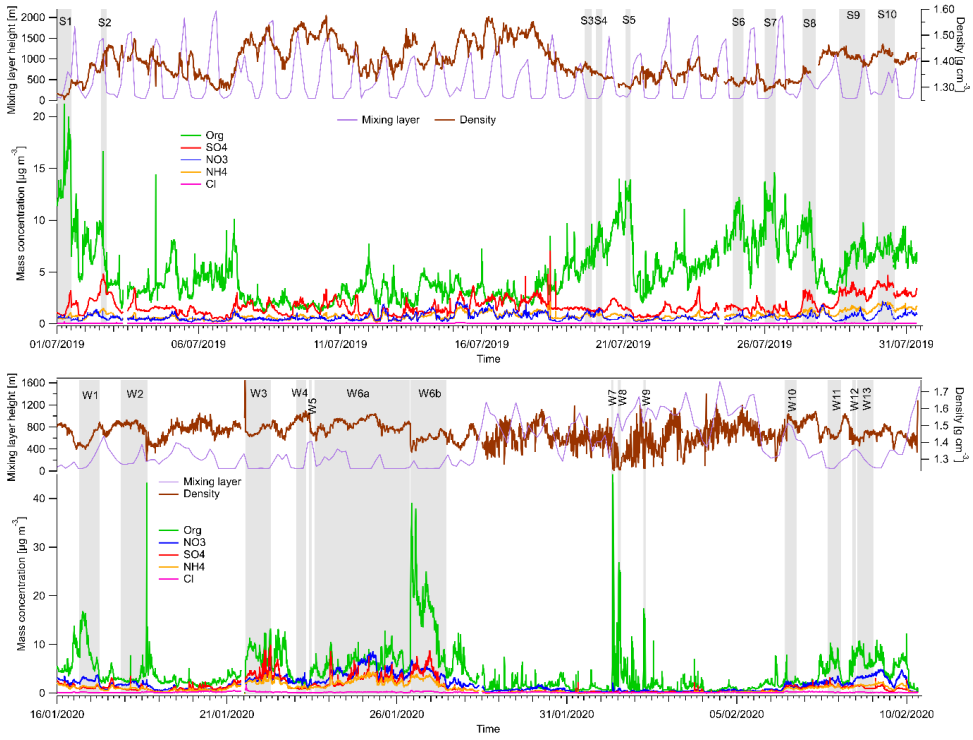

Figure A3. Mass concentration of Org, NO_3^-, SO_4^{2-}, and NH_4^+ measured by AMS with applied constant collection efficiency (CE) correction for summer (top) and winter (bottom) campaign with marked episodes of higher mass concentrations, mixing layer height and particle effective density calculated using Eq. (2) in the main text from Salcedo et al., 2006.

https://doi.org/10.5194/acp-2021-516
Preprint. Discussion started: 14 July 2021

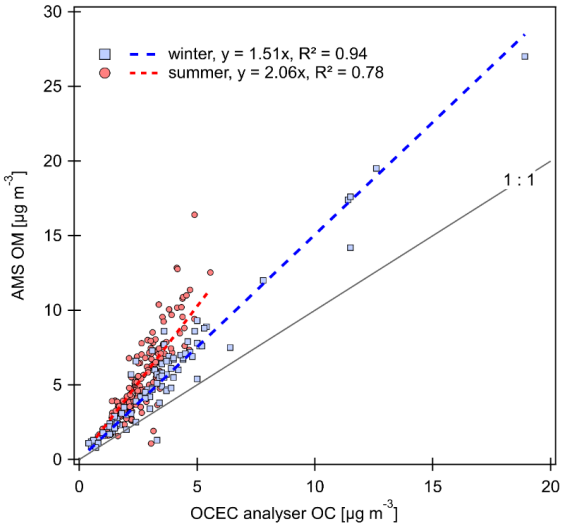

Figure A4. Comparison of organic mass concentration measured on-line by AMS (Org CE corrected) and by OCEC analyser in summer and winter.

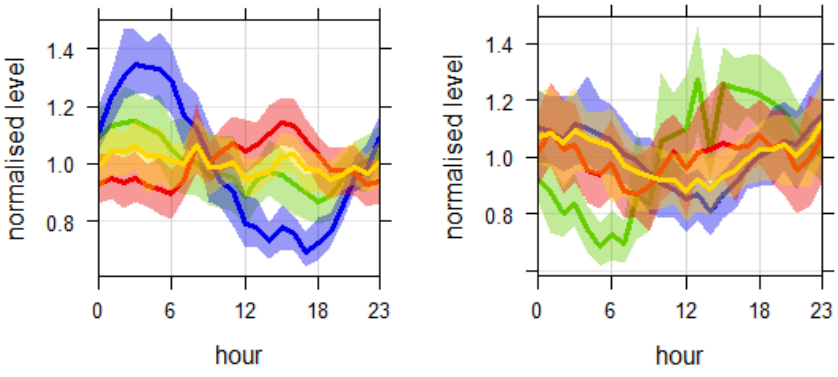

Figure A5. Diurnal trends of the NR-PM_1 species (common colour code) in summer (left) and winter (right).

https://doi.org/10.5194/acp-2021-516
Preprint. Discussion started: 14 July 2021

Table A1. Overview table presenting mass (M) and median diameter (d) of NR-PM_1 species calculated by fitting log-normal function to the AMS size distributions for the selected episodes in summer (S1 – S10) and winter (W1 – 13) along with meteorology recorded during the episodes (relative humidity – RH, global radiation – GR, temperature – T, wind speed – WS and wind direction – WD)

Episode	Start	End	Duration [h]	M_Org [ug m^{-3}]	M_NO_3^- [ug m^{-3}]	M_SO_4^{2-} [ug m^{-3}]	M_NH_4^- [ug m^{-3}]	d_Org [nm]	d_NO_3^- [nm]	d_SO_4^{2-} [nm]	d_NH_4^- [nm]
S1	7.1.19 0:00	7.1.19 12:00	12	14.58	0.82	1.24	0.91	314	285	414	498
S2	7.2.19 13:00	7.2.19 18:00	5	6.33	0.49	4.70	1.52	307	304	325	335
S3	7.19.19 15:00	7.19.19 21:00	6	6.71	2.00	1.84	1.15	373	421	470	453
S4	7.20.19 1:00	7.20.19 6:00	5	8.41	2.03	1.58	1.21	365	388	467	466
S5	7.21.19 2:00	7.21.19 6:00	4	10.83	1.01	1.53	0.95	358	333	473	504
S6	7.24.19 21:00	7.25.19 6:00	9	8.94	0.97	1.59	1.07	284	271	366	412
S7	7.26.19 0:00	7.26.19 9:00	9	9.25	0.98	1.43	0.99	279	253	382	454
S8	7.27.19 8:00	7.27.19 18:59	10	9.63	1.36	3.54	1.56	399	412	439	436
S9	7.28.19 15:00	7.29.19 13:00	22	6.78	1.16	4.49	1.76	409	414	430	439
S10	7.30.19 0:00	7.30.19 14:00	14	9.57	3.37	6.14	2.98	466	491	494	478
W1	1.16.20 15:30	1.17.20 6:00	14.5	8.60	5.63	1.39	3.47	357	378	447	392
W2	1.17.20 21:00	1.18.20 16:00	19	4.04	5.84	1.45	3.83	356	428	456	429
W3	1.21.20 13:00	1.22.20 17:00	28	9.33	7.50	7.13	7.90	563	609	636	607
W4	1.23.20 1:00	1.23.20 8:00	7	1.90	7.04	1.89	4.48	388	386	487	410
W5	1.23.20 10:00	1.23.20 12:00	2	4.26	7.27	3.20	5.46	357	386	433	391
W6	1.23.20 14:00	1.27.20 11:00	93	7.82	9.40	4.18	6.76	460	586	630	588
W6a	1.23.20 14:00	1.26.20 9:00	67	6.18	10.66	4.15	7.55	523	584	629	584
W6b	1.26.20 9:30	1.27.20 11:00	25.5	13.23	6.37	4.34	4.89	398	571	625	593
W7	2.1.20 7:30	2.1.20 9:00	1.5	15.63	0.93	0.74	0.96	336	276	241	390
W8	2.1.20 12:00	2.1.20 14:00	2	10.32	0.72	0.62	0.90	295	240	242	365
W9	2.2.20 6:00	2.2.20 7:30	1.5	10.12	0.17	0.41	0.76	296	787	287	392
W10	2.6.20 10:00	2.6.20 18:00	8	2.15	2.66	4.19	3.35	385	479	473	462
W11	2.7.20 16:00	2.8.20 1:30	9.5	5.76	5.09	2.50	3.30	366	419	488	446
W12	2.8.20 9:30	2.8.20 12:00	2.5	6.52	5.23	2.27	3.06	387	461	523	478
W13	2.8.20 13:00	2.9.20 0:30	11.5	7.72	8.12	1.93	4.35	379	436	498	451

Episode	Start	End	Duration [h]	RH [%]	GR [W m−2]	T [°C]	WS [m s-1]	WD
S1	7.1.19 0:00	7.1.19 12:00	12	49	318	25.8	3.7	W-SW
S2	7.2.19 13:00	7.2.19 18:00	5	44	566	22.8	3.7	N-NNW
S3	7.19.19 15:00	7.19.19 21:00	6	91	92	17.3	1.5	S-SE-W
S4	7.20.19 1:00	7.20.19 6:00	5	97	28	14.9	1.3	SE
S5	7.21.19 2:00	7.21.19 6:00	4	68	31	19.7	2.5	SW-NW

https://doi.org/10.5194/acp-2021-516
Preprint. Discussion started: 14 July 2021

S6	7.24.19 21:00	7.25.19 6:00	9	68	13	18.2	1.2	SW-SE
S7	7.26.19 0:00	7.26.19 9:00	9	59	148	19.1	2.3	W
S8	7.27.19 8:00	7.27.19 18:59	10	75	297	21.3	3.4	SE
S9	7.28.19 15:00	7.29.19 13:00	22	81	156	20.5	2.4	W-NW-SE
S10	7.30.19 0:00	7.30.19 14:00	14	81	196	20.9	3.7	W
W1	1.16.20 15:30	1.17.20 6:00	14.5	92	3	1.1	2.1	SE
W2	1.17.20 21:00	1.18.20 16:00	19	96	13	0.4	2.0	SE-NW
W3	1.21.20 13:00	1.22.20 17:00	28	93	77	-3.8	2.5	W-NW-SW
W4	1.23.20 1:00	1.23.20 8:00	7	88	0	0.1	1.7	W-NW
W5	1.23.20 10:00	1.23.20 12:00	2	73	120	0.6	1.9	SE
W6	1.23.20 14:00	1.27.20 11:00	93	93	34	-1.1	1.7	SE-S-SW
W6a	1.23.20 14:00	1.26.20 9:00	67	94	20	-2.4	2.0	SE-S
W6b	1.26.20 9:30	1.27.20 11:00	25.5	98	43	-1.0	1.1	SE
W7	2.1.20 7:30	2.1.20 9:00	1.5	77	22	9.2	3.9	SW
W8	2.1.20 12:00	2.1.20 14:00	2	69	201	11.9	7.5	SW
W9	2.2.20 6:00	2.2.20 7:30	1.5	75	0	4.1	8.1	W
W10	2.6.20 10:00	2.6.20 18:00	8	76	112	0.4	6.0	W-NW
W11	2.7.20 16:00	2.8.20 1:30	9.5	92	4	0.9	1.5	SE
W12	2.8.20 9:30	2.8.20 12:00	2.5	85	237	0.8	3.9	SE
W13	2.8.20 13:00	2.9.20 0:30	11.5	84	86	0.6	2.7	SE

https://doi.org/10.5194/acp-2021-516
Preprint. Discussion started: 14 July 2021

Atmospheric Chemistry and Physics Discussions

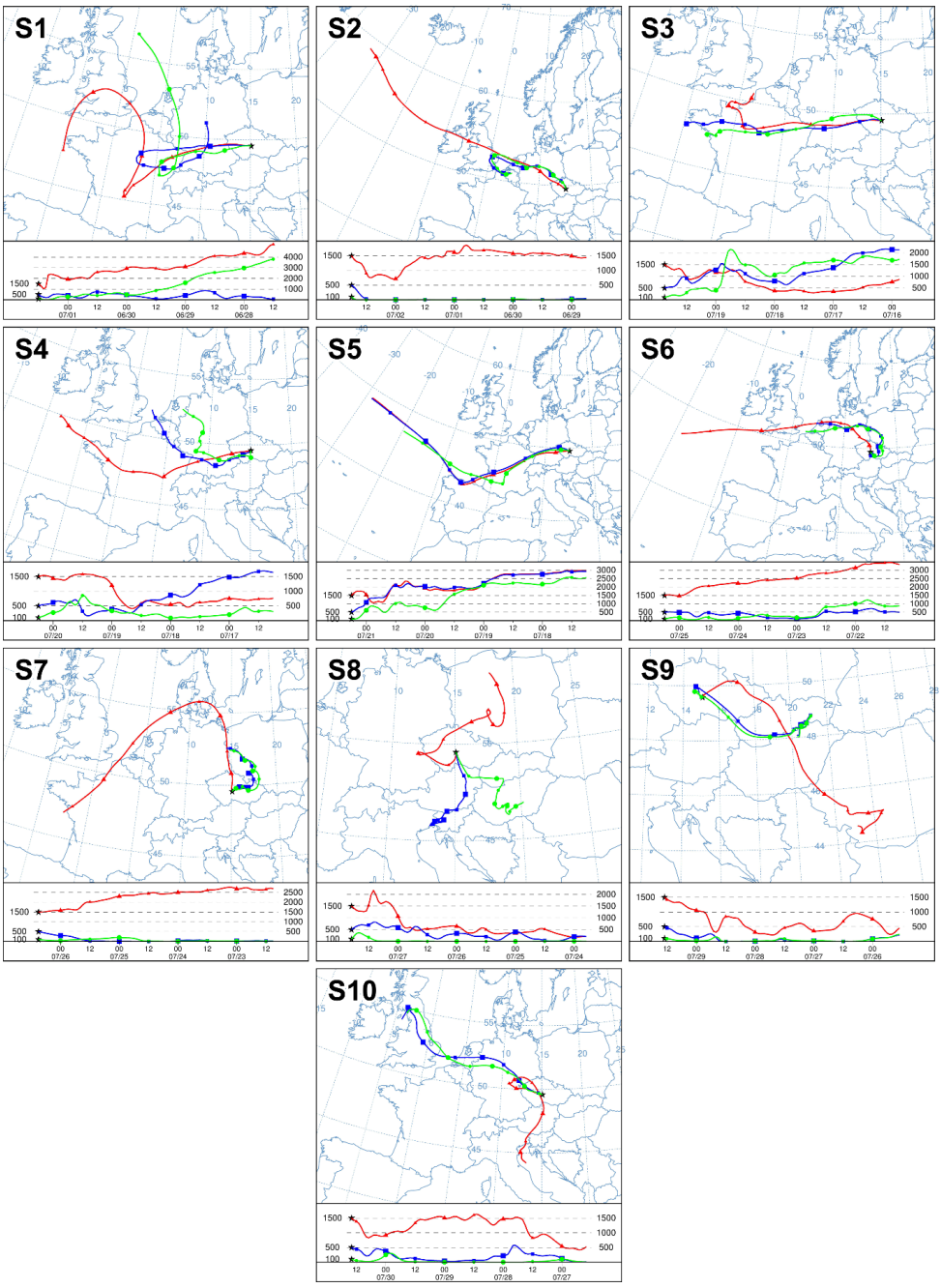

Figure A6. Backward air mass trajectories calculated by HYSPLIT for corresponding summer episodes (S1 – S10) of high concentration of species size distributions.

https://doi.org/10.5194/acp-2021-516
Preprint. Discussion started: 14 July 2021

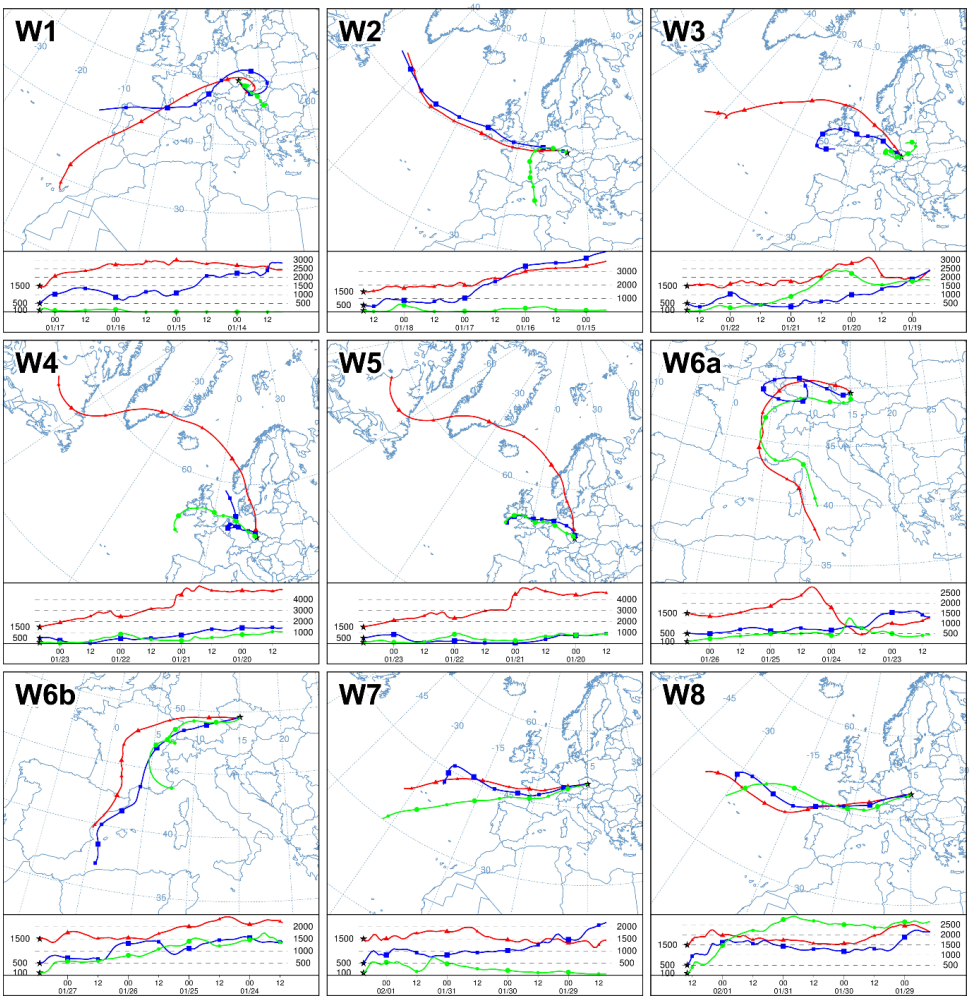

Figure continues.

https://doi.org/10.5194/acp-2021-516
Preprint. Discussion started: 14 July 2021

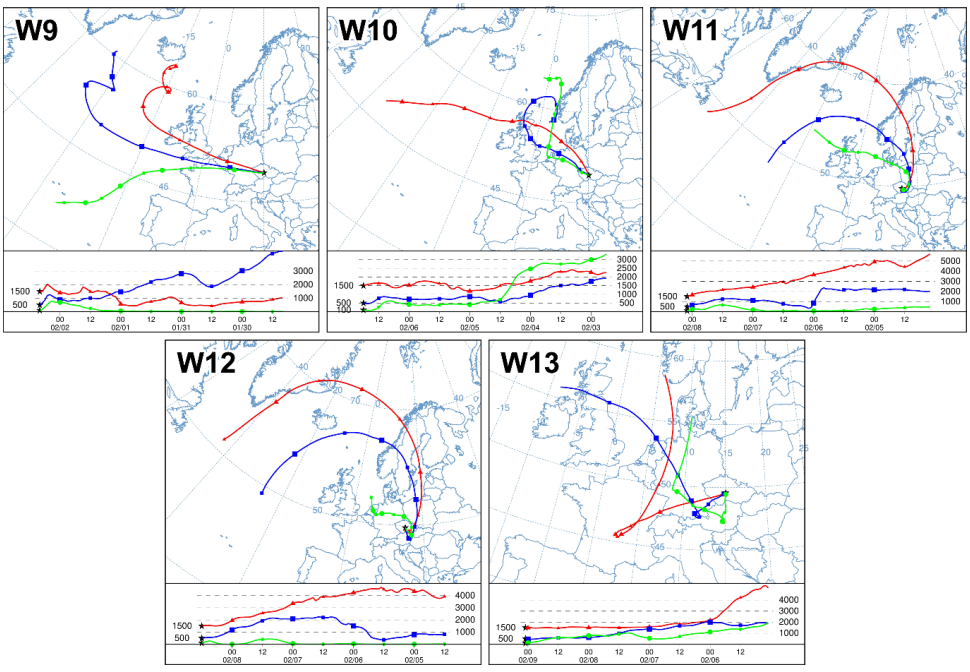

Figure A7. Backward air mass trajectories calculated by HYSPLIT for corresponding winter episodes (W1 – W13) of high concentration of species size distributions.

https://doi.org/10.5194/acp-2021-516
Preprint. Discussion started: 14 July 2021

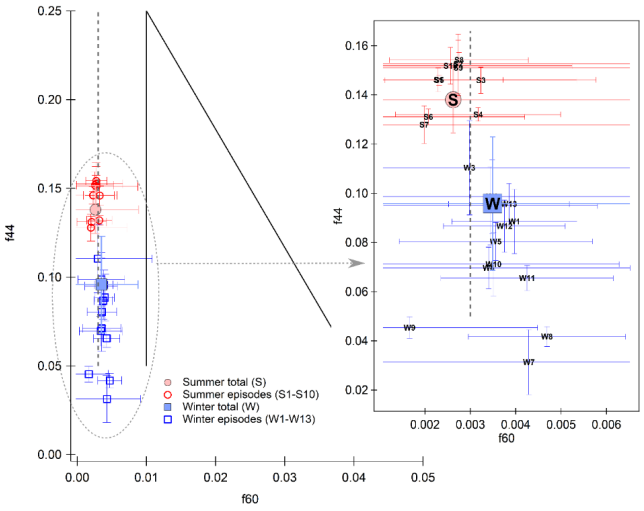

Figure A8. Comparison of organic fragments f_{44} and f_{60} for the whole campaigns (full markers) and for the specific episodes (empty markers). Bars represent standard deviation and the triangular space area of biomass burning (BB) influence and dashed line a limit for a negligible fresh BB influence (Cubison et al., 2011).

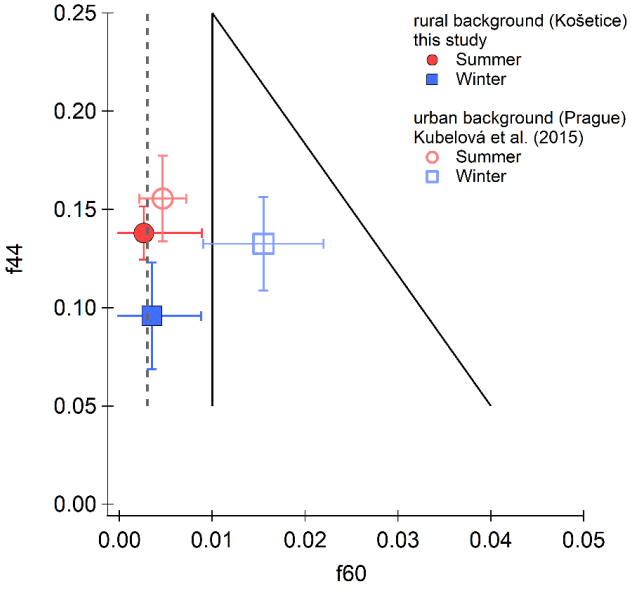

Figure A9. Comparison of organic fragments f_{44} and f_{60} determined at rural background site (NAOK) and urban background site (Prague, study by Kubelová et al., 2015) during summer and winter seasons.

https://doi.org/10.5194/acp-2021-516
Preprint. Discussion started: 14 July 2021

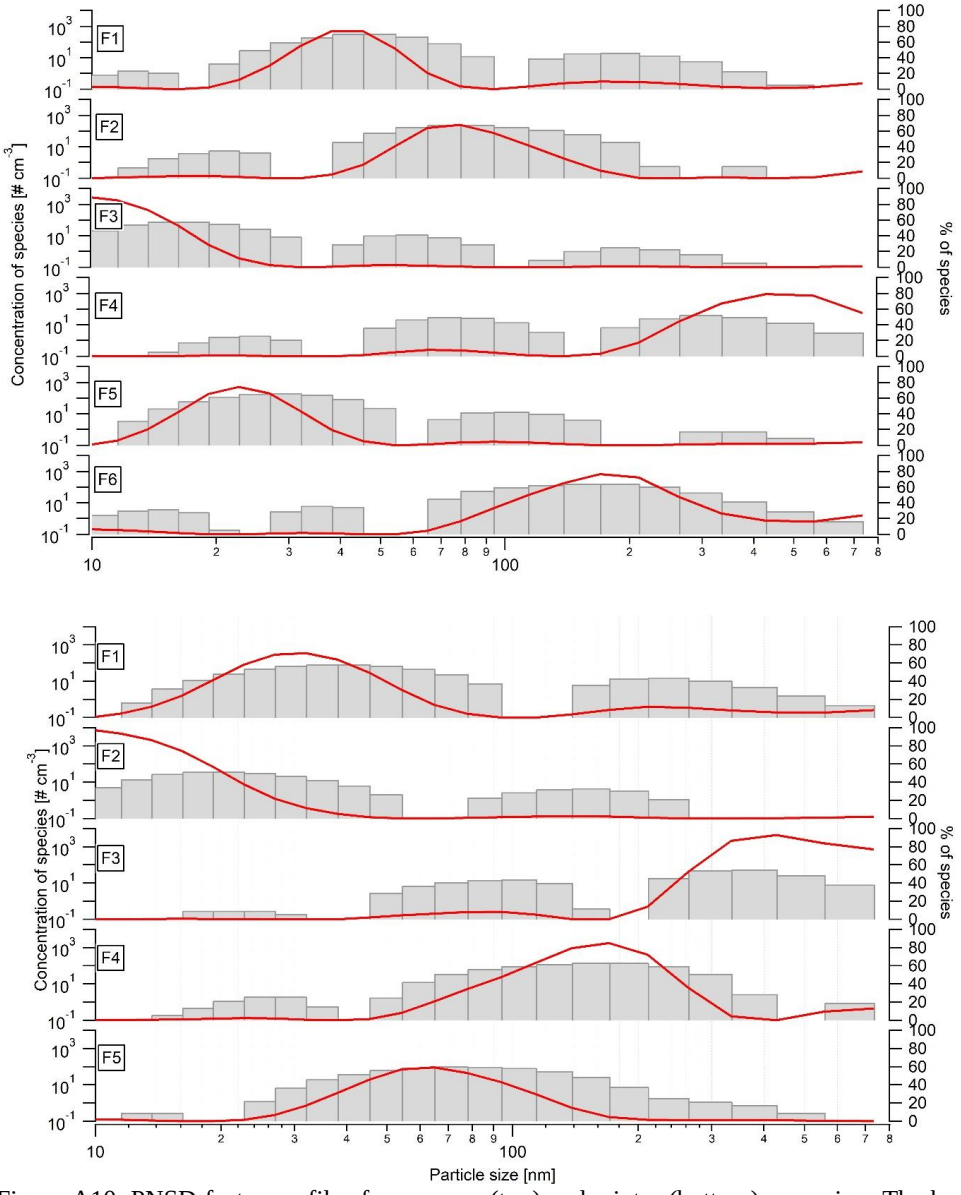

Figure A10. PNSD factor profiles for summer (top) and winter (bottom) campaign. The bars represent the number size distribution (y-axis on the left), and the lines represent the contribution as a percentage (y-axis on the right).

https://doi.org/10.5194/acp-2021-516
Preprint. Discussion started: 14 July 2021

Table A2. Summary of PMF diagnostics for PNSD.

Diagnostic	Summer	Winter
N. of observations	8684	7414
Missing values	6.8%	0%
Number of factors	6	5
$Q_{expected}$	161224	103701
Q_{true}	129774	102925
Q_{robust}	130657	103495
Species with $Q/Q_{expected}>2$	0	263
Extra modelling uncertainty	4.8%	4.0%
DISP swaps	0	0
BS mapping	100%	100%

https://doi.org/10.5194/acp-2021-516
Preprint. Discussion started: 14 July 2021

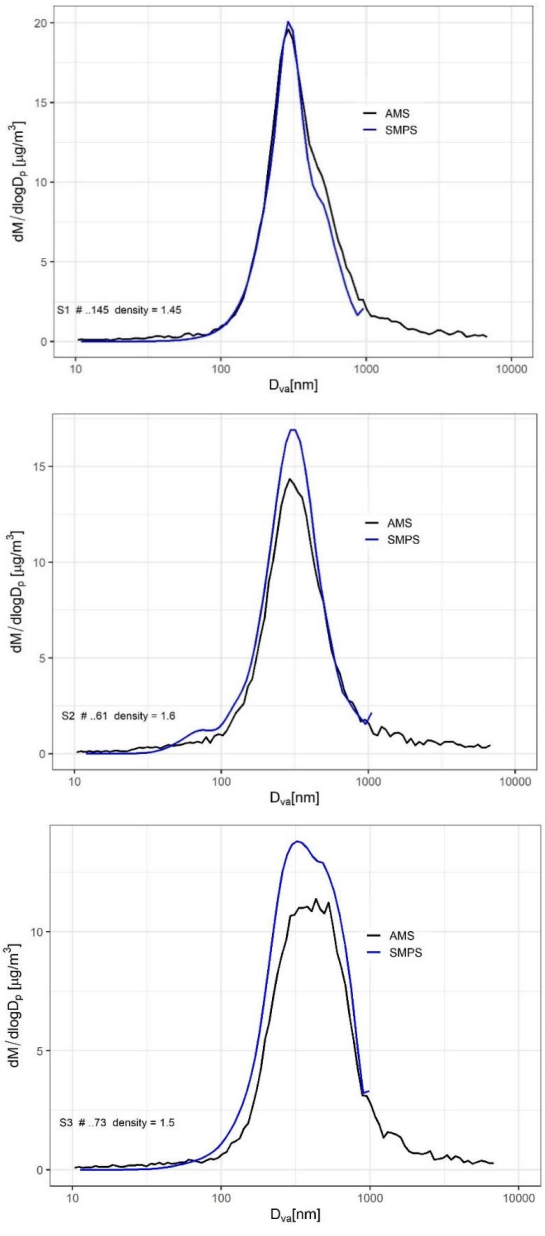

https://doi.org/10.5194/acp-2021-516
Preprint. Discussion started: 14 July 2021

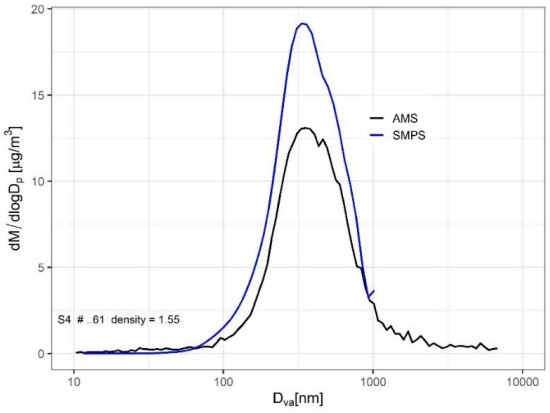

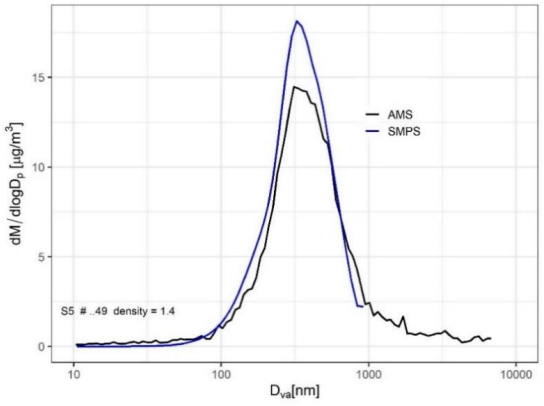

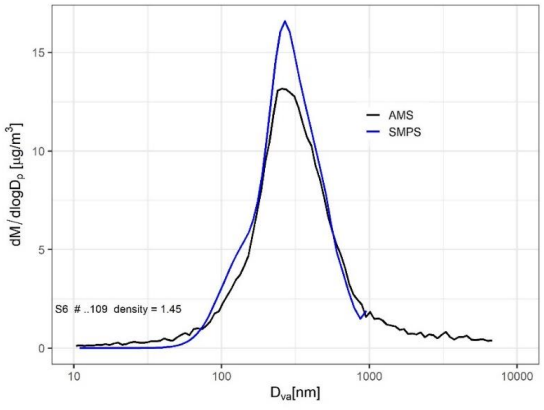

https://doi.org/10.5194/acp-2021-516
Preprint. Discussion started: 14 July 2021

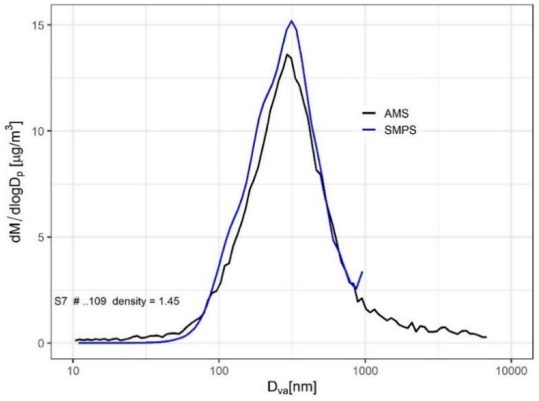

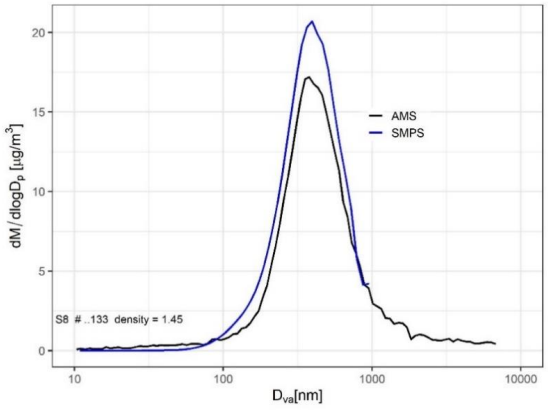

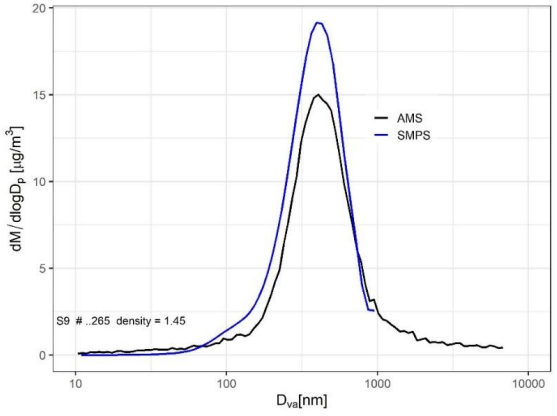

https://doi.org/10.5194/acp-2021-516
Preprint. Discussion started: 14 July 2021

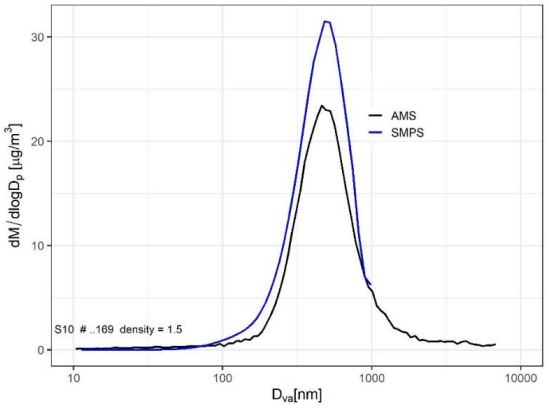

Figure A11. Fit of AMS and MPSS mass size distribution spectra of summer episodes (S1 – S10) for density calculation.

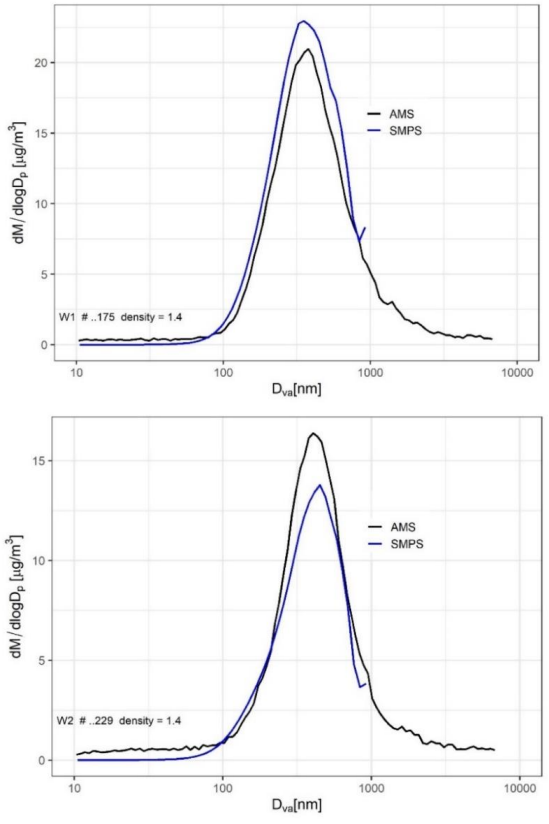

https://doi.org/10.5194/acp-2021-516
Preprint. Discussion started: 14 July 2021

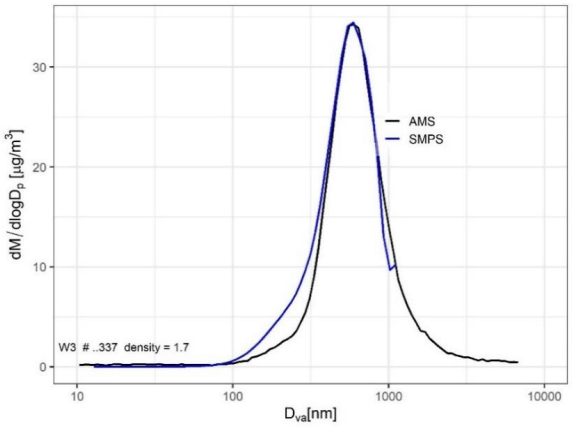

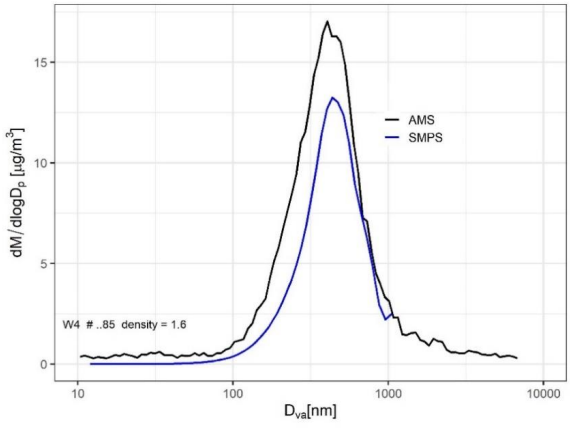

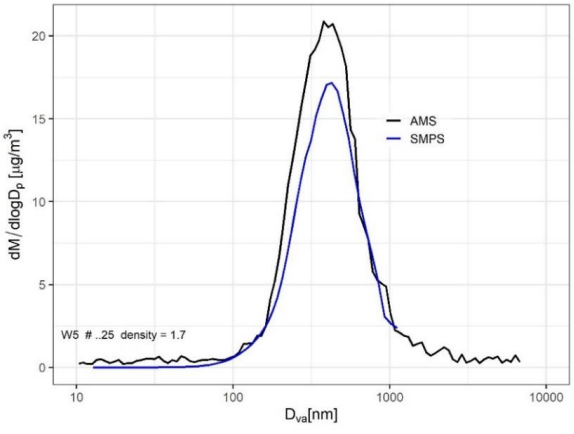

https://doi.org/10.5194/acp-2021-516
Preprint. Discussion started: 14 July 2021

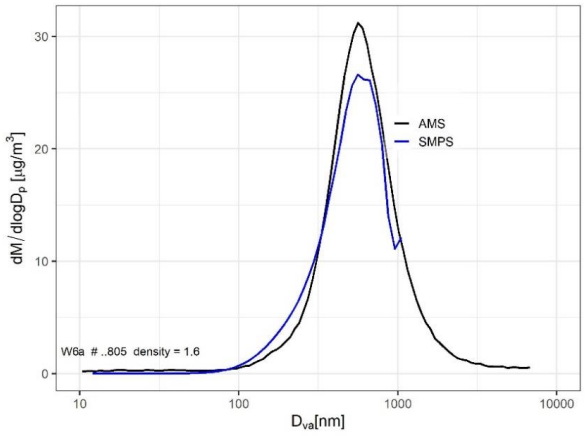

889

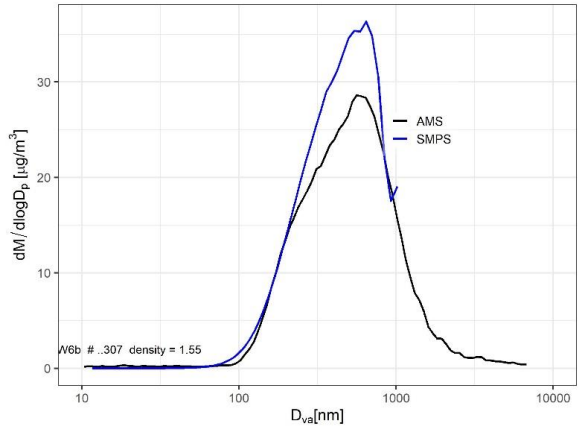

890

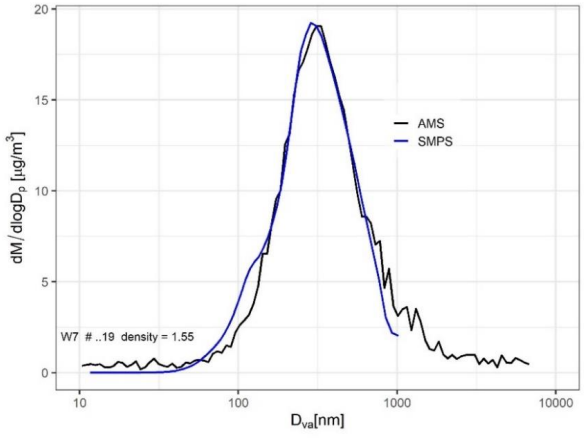

891

https://doi.org/10.5194/acp-2021-516
Preprint. Discussion started: 14 July 2021

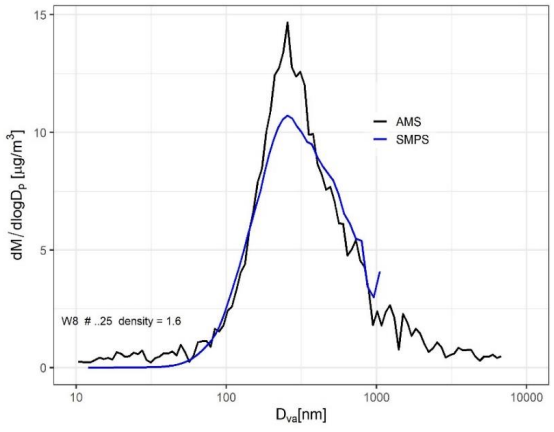

892

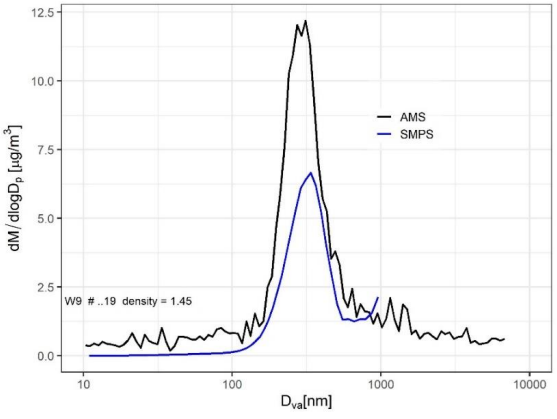

893

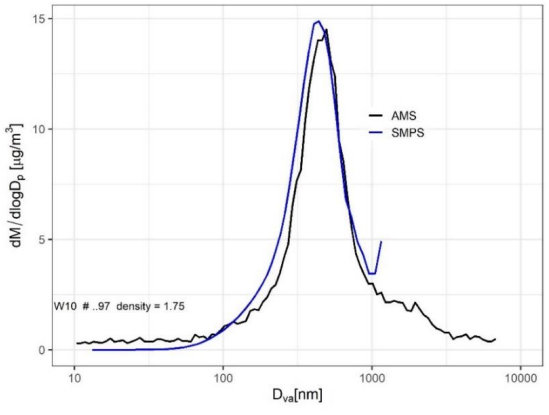

894

https://doi.org/10.5194/acp-2021-516
Preprint. Discussion started: 14 July 2021

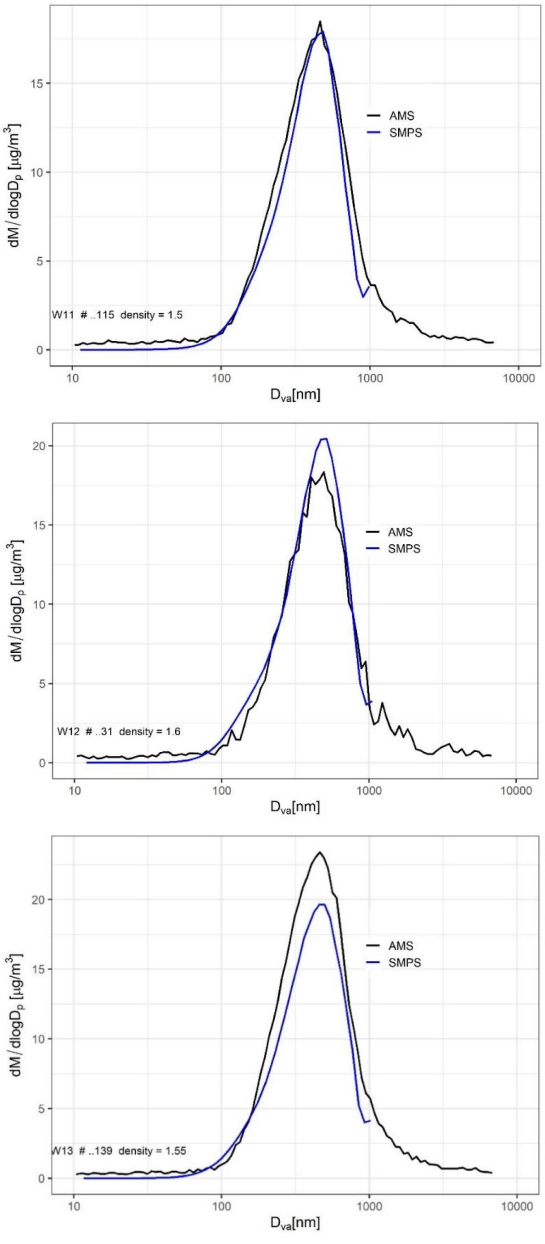

Figure A12. Fit of AMS and MPSS mass size distribution spectra of winter episodes (W1 – W13) for density calculation.

https://doi.org/10.5194/acp-2021-516
Preprint. Discussion started: 14 July 2021

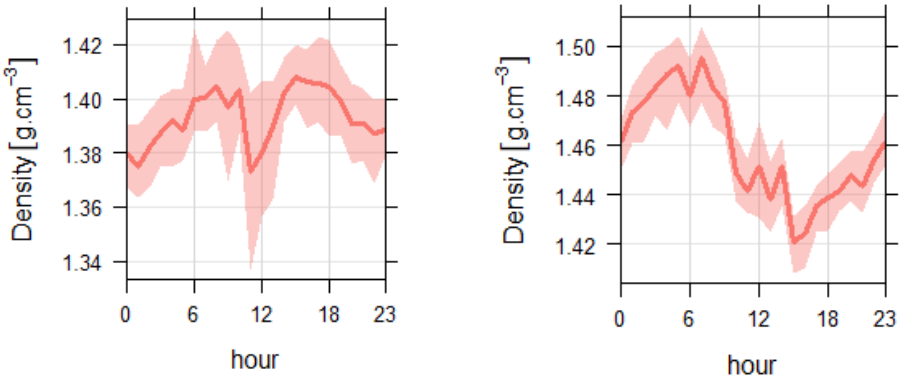

Figure A13. Diurnal trends of average effective particle density calculated based on Eq. (2) in the main text from Salcedo et al., 2006 in summer (left) and winter (right).

https://doi.org/10.5194/acp-2021-516
Preprint. Discussion started: 14 July 2021

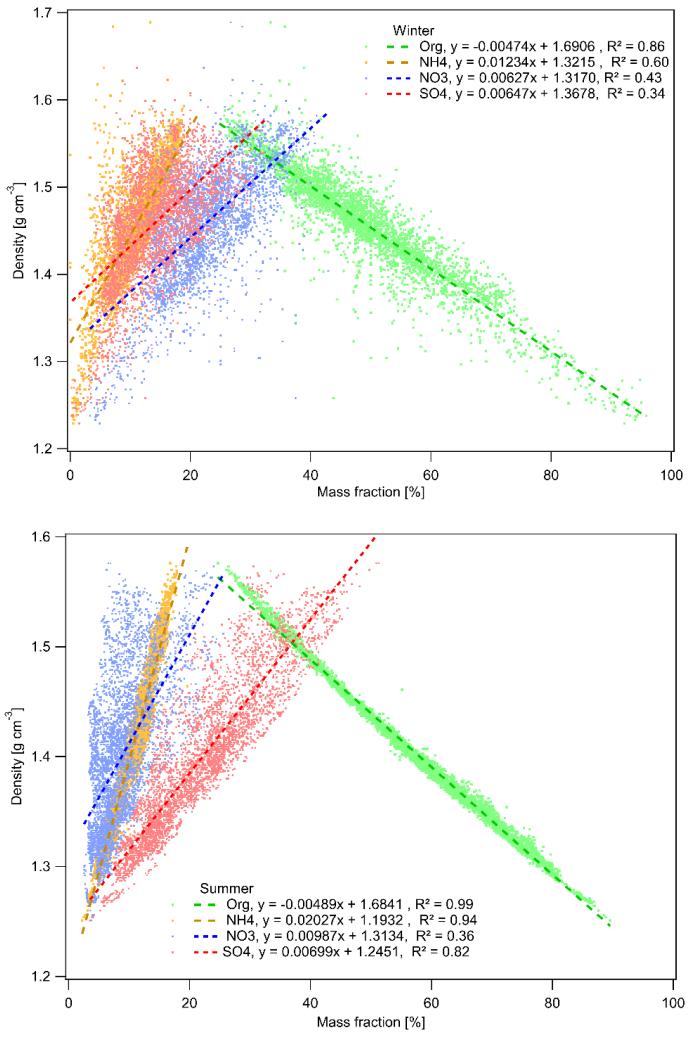

Figure A14. Relationship between density, calculated according to Eq., and mass fractions of the main NR-PM_1 species.